Solar Wind and Interplanetary Magnetic Field: A Tutorial

C. T. Russell

Institute of Geophysics and Planetary Physics and
Department of Earth and Space Sciences
University of California, Los Angles
California 90095-1567

Abstract

The convection layer completes the transport of energy from the nuclear furnace at the center of the sun to its radiation into space by the photosphere, but most importantly for the solar wind it sets the temporal and spatial scales for the structure of the coronal magnetic field that in turn controls the properties of the solar wind. In this tutorial review we examine the properties of the fields and particles that constitute the solar wind and ultimately affect space weather and the underlying physical processes. In particular we discuss the role of the coronal magnetic field; the effect of the rotation of the sun; and the properties of the principal solar wind disturbance at 1 Astronomical Unit, the interplanetary coronal mass ejection.

1. Introduction

There is much about the solar wind that we do not understand as well as we would like to understand. This situation arises because the origin of the solar wind is complex and because the region of solar wind acceleration has not been probed with in situ investigations. In contrast we know much about the solar wind at the orbit of the Earth. It flows with a speed of about 400 km s^{-1} and a density of 5 cm^{-3}. It carries a magnetic field of about 5 nT that lies near the ecliptic plane in an Archimedean spiral pattern and it is highly variable.

Addressing the solar wind from first principles is also difficult because the solar wind is a magnetized plasma in which, throughout most of the solar system, the magnetic and plasma pressures are comparable. Often our intuition, trained on the behavior of gases, fluids and

magnetic fields in a vacuum, does not strictly apply in a plasma like the solar wind. To treat this regime properly many approaches have been tried, each with a different approximation and with minimal guidance from observables in the critical regions. The fluid approximation assumes that the plasma can be treated by examining the behavior of moments of the distribution such as density and velocity. The behavior of the fluid is governed by a set of equations including Maxwell's laws, for the electromagnetic quantities, and the conservation of mass, momentum and energy, and possibly higher order moments. Frequently these equations are truncated by setting the high order moments to zero and the equation of state of an ideal gas becomes the energy equation. Here $P\rho^{-\gamma}$ is constant where P is the pressure, ρ is the mass density and γ is the polytropic index. This closure in fluid treatments is often arbitrary and based on analogies with ideal gases that may not apply. Further a decision on the number of components of the plasma that need to be separately treated must be made. Should ions and electrons be treated separately? Should different ions be considered separately? Is there more than one population of electrons or ions that requires a separate treatment? Thus even a fluid treatment of the solar wind can be cumbersome. Kinetic treatments avoid some of these difficulties [*Meyer-Vernet*, 2000] but may lead to tractable solutions in only simple geometries. The caveats about the number of components that may be important in a plasma applies equally well to kinetic treatments. As a result unlike many areas of space physics, our understanding of the solar wind is founded on long term observations rather than a solid foundation of theory.

In addition to being unable to decide a priori the number of components of the solar wind that control its behavior, there is controversy as to whether the solar wind can be treated as a Maxwellian or not and even whether fluid theory can be applied. In a collisional gas the phase space distribution, the number of particles per unit of configuration and velocity space tends

toward a Maxwellian distribution. Maxwellians have special properties that make them simple to use, but plasmas are not always Maxwellian. Thus one must be very careful about applying theories or equations that may implicitly assume Maxwellian behavior. To rectify this problem some authors approximate space plasmas with Lorentzian distributions that have a high-energy tail, characterized by a value, kappa. For a kappa of infinity the Lorentzian distribution becomes Maxwellian. The Lorentzian distribution can be used in a fluid approach, and so it is not strictly correct to call plasma studies kinetic just because they use a non-Maxwellian distribution. Nevertheless, this is often done in the literature, adding ambiguity to the use of the term "kinetic" treatment. As we will see below when we examine the detailed properties of the solar wind, the observed behavior of the solar wind may be very strongly affected by its non-Maxwellian distribution.

The energy of the sun derives from the conversion of mass to energy when hydrogen atoms are converted by fusion to helium and helium converted to carbon. This energy is radiated from the core into the layers above. At about 0.75 solar radii (R_s) heat transport by radiation drops in efficiency below that of convection and, the outer layer transports the escaping heat to the surface by convection. This mass motion results in cooler material sinking from the photosphere into the convection layer and hot material rising toward the photosphere. The mass motion drives the magnetic dynamo that we see on the sun and whose time variations are so very important for solar terrestrial relations.

The time scale for the transport of heat from the interior of the Sun is millions of years while the time scales in the photosphere range from hours to years. Once heat reaches the photosphere it radiates to the Earth at the speed of light reaching 1 AU in about 8 minutes or convects in the solar wind at about 400 km s^{-1} reaching the Earth in about 4 days. In this review

we examine the behavior of this magnetized solar wind plasma. We discuss its behavior beginning with the simplest possible model: a spherically symmetric, non-magnetized, non-rotating and time-stationary star. Next we examine those properties that are affected by its magnetic field, those associated with rotation, and finally those associated with the time variation of the system. We hope that, by dividing the phenomena this way, a greater understanding of the ultimate causative mechanisms may be more readily obtained.

Finally, we note that the solar wind is important for very practical as well as academic reasons. For those interested in space weather, the interaction of the solar wind with the Earth's magnetic field is very important. The solar wind both controls the size of the magnetic cavity through its momentum flux or dynamic pressure and the energy flow into the magnetosphere coupled from the solar wind mechanical energy flux by the reconnection of the interplanetary magnetic field with the terrestrial field. This coupling is strongly controlled by the direction of the interplanetary magnetic field, being most strong when the interplanetary magnetic field is southward. Thus for space weather applications we are most interested in the solar wind velocity and mass density and the strength and orientation of the interplanetary magnetic field. Nevertheless, the interaction with the Earth is complex and other parameters such as temperature are important as well.

2. The Solar Wind Plasma

The temperature of the photosphere is less than 6000K and as a result the sun is most luminous in what we call visible light. The temperature at first falls and then rises rapidly as one moves above the photosphere as shown in Figure 1. This behavior is reminiscent of the behavior of the upper atmosphere of the Earth, in which the absorption of solar photons in the stratosphere and the thermosphere create warm layers well above the surface of the Earth. Here too the

corona appears to be a region of heating from which heat is conducted downward to the chromosphere below and convected outward from the corona by the solar wind. Understanding the source of this coronal heating is one of the outstanding problems of the solar wind.

The high temperature of the corona is important since the solar wind must escape the deep gravitational potential well of the sun. The escape velocity is 625 km/s from the surface of the sun. Thus a proton requires over 2 keV to escape to infinity from the surface of the sun and about 0.5 keV to escape from 5 R_s. The thermal energy of a 10^6 K proton is only about 100 eV. Understandably there was some doubt expressed before the advent of the first in situ solar wind data about the feasibility of a continual high speed solar wind, but *Parker* [1958] predicted such a wind based upon hydrodynamic theory and the long term observations of Mariner 2 confirmed its reality [*Snyder et al*., 1963]. Figure 2 shows the results of an isothermal fluid treatment of the expansion from the corona as first described by Parker [1958]. Because the pressure gradient falls off with radial distance more slowly than the gravitational force the solar wind is accelerated even to supersonic velocities. The Earth sits about 230 R_s from the sun. As Figure 2 illustrates, the solar wind has achieved close to its asymptotic velocity by the time it reaches 1 AU. For a coronal temperature of close to 10^6 K the observed median solar wind velocity is obtained in this solution. Nevertheless, modeling the solar wind expansion is still an active area because we have few observational constraints on the nature of the "heating processes" in the acceleration region. In part because of the weakness of our understanding of the solar wind in those critical regions of the corona where we have not been able to obtain in situ data we concentrate in this review on solar wind phenomenology at 1 AU.

2.1. Ions

Most solar wind instruments flown to date return counts versus energy per charge which

can be interpreted as counts per increment of velocity times square root of mass/charge as shown in Figure 3. In this particular example we see that there are four beams: two proton beams and two alpha beams. In a magnetized plasma the bulk velocity of all particles perpendicular to the field must be equal. The bulk velocity along the field need not be so, and here it is clearly not equal. The reason for such differences must still be speculative, but since interpenetrating ion beams are not rare, it is important to understand their origin. The widths of these peaks are narrow compared to the energy of the peak. Thus the thermal velocity of the particles (the random component perpendicular to and parallel to the magnetic field) is small compared to the bulk velocity. This is an indication that they are supersonic. They move faster than the speed of a sound wave in the plasma. They also move faster than the magnetosonic velocity that is a combination of the sound and Alfven speeds. Not as obvious here is the fact that the alpha particles have temperatures about four times greater than those of the protons. In fact all ions have temperatures that on average are roughly proportional to their atomic mass, i.e. their thermal velocities are roughly equal [*Boschler et al*., 1985]. This relationship, however, is not strictly obeyed. Coulomb collisions tend to equilibrate these temperatures, especially when the ion temperatures are low [*Klein et al*., 1985]. Thus deviations from this relation are found in cool dense solar wind flows and He^{++} cools more rapidly with heliocentric radius than protons [*Thieme et al*., 1989].

The distribution shown in Figure 3 is a one-dimensional cut along the direction toward the sun. A rapidly spinning single detector can resolve a two dimensional or angular distribution, and, if it has multiple sensors such as on Helios, a three-dimensional spectrum can be measured. Since charged particle distributions are usually cylindrically symmetric around the magnetic field (gyrotropic), the angular distribution can be displayed, as in Figure 4, by

displaying the flux parallel and perpendicular to the magnetic field. The angular distribution of the solar wind ions is complex, often with quite different shapes in the directions parallel and perpendicular to the magnetic field. Sometimes the contours are elliptical with their greatest dimension along the field, so that $T_{\|}>T_{\perp}$. In other cases the contours are elongated perpendicular to the field, so that $T_{\perp}>T_{\|}$.

If we assume that the entropy of the solar wind ions does not change as the ions move outward then we can relate pressure and density by the polytropic law $P\rho^{-\gamma}$ = constant. For P=nkT, this translates to $n^{(1-\gamma)}T$ being constant. Since γ is greater than unity, T decreases as N decreases. As the solar wind expands radially, and roughly spherically, its density falls off as r^{-2}. We therefore expect the solar wind temperature to fall as the solar wind expands and it does. In a collisionless magnetized plasma, in the absence of fluctuations both near the gyrofrequency and at magnetic scale sizes near the gyro radius, the first adiabatic invariant, or magnetic moment, of the ions will be conserved. Thus, the perpendicular energy of the ions divided by the local magnetic field strength would be constant, and as the ions propagate outward, their pitch angles would become more field-aligned. This behavior is indeed seen qualitatively, but not quantitatively. There is heat transport along the field and dissipation. Wave particle interactions couple the parallel and perpendicular ion temperatures in the solar wind and limit the ratio of these two temperatures as the solar wind expands. The slow solar wind that is denser and has a longer transit time cannot be assumed to be completely collisionless. The observed distributions are also affected by the electric potential of the solar wind. In the fast solar wind for reason we do not completely understand the temperatures are more isotropic than they are in the slow solar wind.

At the Earth the solar wind is highly variable. In sections 3-5 we discuss the various processes that lead to this variability but here we concern ourselves just with the statistical properties. Figure 5 shows a histogram of the solar wind velocity. It can be as slow as 260 km s^{-1} and faster than 750 km s^{-1}, but typically lies about 400 km s^{-1}. Figure 6 shows the density. It is much more variable than the velocity, ranging from about 0.1 cm^{-3} to 100 cm^{-3}. Thus variations in the dynamic pressure with which the solar wind blows against the magnetosphere and the size of the magnetosphere are controlled principally by the density fluctuations. The factor of three change in the velocity makes a ± 20% change in the radius of the magnetosphere, but the range of density makes a ± 80% change. Over the solar cycle the yearly average dynamic pressure changes about ± 20% [*Petrinec et al.*, 1991]. This makes a small but perceptible (± 3%) change in the size of the magnetosphere. When high densities and high velocities occur together the size of the magnetosphere can be halved, but in general the density of the solar wind and the velocity are inversely correlated as shown in Figure 7. While it is often said that the number flux is roughly constant, the line of constant flux shown in Figure 7 indicates that this constant flux rule is only a rough approximation. In contrast the ion temperature is positively correlated with the solar wind velocity as shown in Figure 8. This correlation is certainly qualitatively consistent with the Parker's model of solar wind expansion illustrated in Figure 2.

2.2. Electrons

Although frequently it is possible to treat ions as a single fluid in the solar wind, this is not true of electrons. Electrons most frequently appear to have at least two components, a core and a halo. As shown in Figure 9, the core is colder than the halo and it is denser. It is important also to note that the thermal speeds of both populations are greater than the solar wind bulk speed. Thus the electrons can leave the sun much faster than the ions although in the direction

perpendicular to the magnetic field they drift together at the same velocity. A paradox is introduced by this difference in velocity that arises because in the corona the ions and electrons have similar temperatures but very dissimilar masses. In a collisionless gas, like the solar wind over most of its transit from the sun, charged particles do not leave their magnetic field lines. They also maintain quasi charge-neutrality. How can they do this if they are not traveling at the same speed? The answer is trivial if the source regions on the sun are constant in time so that the flux of electrons and ions at the base of a field line is constant. The density is always the same and it does not matter if the protons and ions stream relative to each other along the field. If the solar wind production rate varies in time and the ion density along a flux tube varies with distance, then the electrons have to slow down as they pass through dense regions and then speed up in rarefied regions. This occurs because when there is an over abundance of ions there will be a polarization electric field that attracts the electrons to that region. In regions of under dense ions the electrons will be expelled by the excess negative charge. As a result, charge imbalances are minimal in the solar wind despite the speed differences and time variations. We might expect variations in the electric potential along the magnetic field but no detectable variation in charge neutrality. Because the core electrons travel most slowly they are affected the most by these electric potential variations, and the overall electric potential surrounding the sun.

Figure 10 shows angular distributions of the solar wind electrons and cuts through these distribution functions. Sometimes the electrons can be nearly isotropic. At other times, not only is there the core and halo distribution but also a narrow field-aligned high energy beam that is called the “strahl”. Since the collision frequency of charged particles is inversely proportional to square of the particles’ energy, the high energy strahl can propagate farthest without scattering. In some sense the strahl provides a look at the deepest part of the corona. As with the ions we

expect gyrotropy about the magnetic field direction, and as with the ions there is great variability in the shapes of the distributions. In stark contrast to the ions the electrons have a nearly constant temperature when averaged over the distribution function which is dominated by the denser core electrons. Figure 11 illustrates this constancy versus the solar wind velocity. This constancy occurs in part because the electrons are strongly coupled to the corona by their high thermal velocities. When they do get heated in the solar wind, say by the passage of a strong shock, they rapidly (in hours) return to their typical temperatures. The main exception to this rule is when the ions are exceptionally hot. This controlling factor is shown by the plot of electron temperature versus ion temperature in Figure 12. If the electron and ion temperatures were completely independent then the distribution of electron temperatures would be the same at each ion temperature. This is largely true except at the lower edge of the electron distribution where a cutoff occurs that moves to higher electron temperatures as the ion temperatures rise. Since we know of no waves that can couple the electrons and ion thermal energies we are left to speculate that the electric potential of the solar wind must in some way be doing this coupling.

We have stressed in this review the non-Maxwellian nature of the solar wind electron and ions. One might think this could have but a minor effect on the behavior of the particles, perhaps because of wave-particle interactions. However, the non-Maxwellian nature of the distributions may have a very important and non-intuitive effect on the plasma. Figure 13 plots Maxwellian and a Lorentzian distribution functions f(E) as a function of energy E showing their evolution with height in a potential that is pulling the particles down. When the Maxwellian particles rise to altitude, Z, and thereby lose potential energy, W, their distribution function has the same shape. When the particles with the Lorentzian distribution rise, the distribution function has a new slope near zero energy because the slope of the original Lorentzian varied with energy. Thus

the temperature at high altitude appears to be greater.

The gravitational field of the sun is an attractive potential. This potential is modified because the electron thermal speed greatly exceeds the bulk velocity of the ions. In a vacuum the sun would charge up positively to keep the electrons in check and to give the ions a boost. This does happen in a plasma but only over a Debye length. In the solar wind an ambipolar electric field appears that maintains charge neutrality and modifies the gravitational potential. *Scudder* [1992] has used this potential plus Lorentzian particle distribution functions to produce a rise in temperatures in the corona without any additional source of heat. Figure 14 shows the electron and ion temperatures as a function of distance for a particular Lorentzian distribution [*Scudder*, 1992]. A strength of this model is that the temperature of heavier than the average, non-Maxwellian ions should increase as their potential energy, proportional to their mass, and such an increase is seen [*Scudder*, 1992; *Meyer-Vernet*, 2000]. This hypothesis for explaining solar wind properties is the subject of much controversy. If indeed this model were to explain the temperature of the corona, it still has not solved the main solar wind problem, as it does not specify how the non-Maxwellian distributions are produced, only how they evolve. The various postulates about the roles of waves, small scale reconnection and other micro processes in the corona are relevant to either the Maxwellian or Lorentzian approaches.

We cannot presently probe the inner corona directly to measure its electron distributions, but the Earth's magnetosphere surprisingly gives us a way to recreate at least some of the coronal electron distribution function. Figure 15 shows the phase space density of "polar rain" energetic electrons, measured on open tail field lines connected to the polar cap, as a function of electron energy [*Fairfield and Scudder*, 1985]. These originally solar-wind electrons have entered the magnetosphere by reconnection of the interplanetary magnetic field with magnetotail field lines.

In the tail and especially at low altitudes the magnetic field increases to values approaching those in the corona and the pitch angle distribution present in the corona can be recreated. This mapping is negatively affected by collisions, and these are greatest when the solar wind is densest. Thus we would expect the greatest anisotropies to survive when the solar wind is least dense and because scattering is least at highest energies the anisotropy should be greatest at highest energy. Figure 15 shows that, when the solar wind density is greatest, the polar rain and the solar wind strahl are weakest and, when the density is least, the strahl and polar rain are most intense as evidenced by the high energy tail on the distributions. When the solar wind density gets extremely low as it did for example on May 11, 1999, the strahl and the polar rain can become intense enough to cause x-ray auroras over the polar cap [*D. L. Chenette*, personal communication, 1999].

3. The Solar Wind Magnetic Field

Processes inside the sun break its temporal and spatial homogeneity, creating an ever-changing photosphere. An important element of this spatial and temporal inhomogeneity is the presence of a magnetic field generated at the base of the convection layer that extends high into the corona and the solar wind. This magnetic field in turn affects the spherical symmetry of the solar wind expansion and suppresses that expansion in some places. Figure 16 shows both an undisturbed dipole field and isothermal MHD coronal expansion model of *Pneumann and Kopp* [1971]. The dipolar magnetic field in this model keeps the equatorial corona tied to the sun. At higher latitudes the solar wind expands along the magnetic field, carrying the solar wind field into interplanetary space from the polar regions of the sun and creating a heliospheric current sheet between the two polar coronal hole outflows.

This magnetic pattern is usually not symmetric about the rotational axis of the sun nor is

it purely dipolar. In the latter case the heliomagnetic equator that separates inward and outward interplanetary magnetic field is warped. Thus, as the sun rotates, the pattern set by the Sun's field sweeps over the Earth causing the magnetic sectors seen in the interplanetary magnetic field as illustrated in 3D perspective in Figure 17. Furthermore, the Earth's orbit is not in the rotational equator of the sun so that in the course of a year the Earth spends six months above the rotational equator and six months below it. As illustrated in Figure 18 these excursions can result in a spacecraft in the ecliptic plane seeing predominantly inward and then predominantly outward fields six months later, but on average the magnetic field is nearly equally inward and outward.

For the reasons discussed in section 4 the angle that the magnetic field makes in the solar equatorial plane or the ecliptic plane lies mainly along a spiral, but the angle of that spiral can vary over the full range of 360^{o}. The occurrence rate of this spiral angle for three sets of solar conditions and at two heliocentric radii are given in Figure 19 [*Luhmann et al.*, 1993]. We note that for the reasons discussed in section 4, the spiral angle at 0.7 AU is closer to 0 and 180 (radially toward and away from the sun) than it is at 1 AU. This plot also demonstrates the very near equality of the occurrences of magnetic fields toward and away from the sun.

The magnitude of the solar wind magnetic field is also quite variable as illustrated in Figure 20 again for two heliocentric distances and three levels of solar conditions. It is clear that the distribution is not Gaussian but that it has a long high amplitude tail, especially so at active times. This behavior is reflected in the components of the field shown in Figures 21, 22 and 23. Note that here the 0.72 AU measurements for the three components, Bx, By and Bz have been adjusted to 1.0 AU both to be more easily compared with the IMP 8 and to be more relevant to space weather applications. We see again that the strongest fields occur at solar maximum when

there is a high field tail on the distribution. These high fields are almost exclusively due to interplanetary coronal mass ejections that are discussed in Section 5. We note that the shape of the Bx and By distributions differ from the shape of the Bz distribution near zero strength components. This occurs because the sector pattern causes the Bx and By components to be distributed around two modal values, one negative and one positive, while the Bz component is distributed around zero. Further there is some evolution in the distributions as the magnetic field is carried from 0.7 to 1.0 AU. We attribute the appearance of more high fields at 1 AU than in the adjusted 0.72 AU distribution as due to the interaction of fast and slow streams as the solar wind moves from the orbit to Venus to that of Earth.

The closed magnetic regions allow the corona to build up in density and temperature in the magnetic equatorial or streamer belt region, as sketched in Figure 24 and as seen in coronographs or with the naked eye at the time of eclipses. In the coronal hole regions on the sun, from which the solar wind flows freely and whose magnetic field lines are open, are called coronal holes. In these regions the density is lower and the temperature cooler. The connectivity of coronal holes and the more distant solar wind has been demonstrated by tracing field lines back to the sun with an MHD model [*Linker et al*., 1999]. The model also reproduces the intensity variations seen in the streamer belt of the lower corona and has been used to predict the appearance of the sun during total solar eclipses.

Since the streamer belt is nearly equatorial at least at solar minimum, the slow solar wind is on average found near the ecliptic plane and the fast solar wind at high latitudes. Ulysses measurements out of the ecliptic plane [*McComas et al*., 1998] and shown in the accompanying paper by *Gosling* [2000] emphasize what a biased sample the Earth receives of the solar wind. The latitudinal profile of the solar wind velocity measured by Ulysses suggests that there is a

dichotomy of solar wind properties organized around the heliospheric current sheet with dense low speed, solar wind near the equatorial regions and rarefied fast flows at high latitudes. However, even though solar wind properties such a composition are ordered by the solar wind speed, this control appears as a continuous change and there is no sudden change in properties at some particular speed. Again using MHD models to extrapolate the solar wind back to its solar source puts the origin of the fast solar wind in coronal holes and the slow solar wind at the edges of coronal holes [*Neugebauer et al*., 1998]. A corollary of this magnetic control of the solar wind expansion is that the flux tube divergence of the magnetic field measured at the source surface correlates well but negatively with the solar wind speed [*Wang and Sheeley*, 1990]. Where coronal magnetic flux tubes are straight and radial the solar wind is fast and where they strongly diverge the solar wind is slow. During solar maximum coronal holes and regions of flux tube divergence are more evenly spread over the Sun's surface than at solar minimum, allowing the Earth to experience a broad range of solar wind velocities, almost independent of its heliographic or heliomagnetic latitude. During the declining phase of solar activity when the current sheet has a large tilt to the solar equator but there is more order to the coronal fields, a more stable fast/slow steam structure arises. It is possible that some slow solar wind arises in the coronal streamer belt [*Gosling*, 1997] but this source is not expected to provide as steady or as wide a region of slow solar wind as that observed.

A solar terrestrial consequence of this control of the solar wind by the magnetic structure of the sun could be that in the course of the year, as the Earth moves from near the Sun's rotational equator to higher (7^{o}) latitudes on roughly March and September 5 each year, it might encounter more frequent high speed solar wind and hence encounter greater geomagnetic forcing. However, there is a second annual variation that affects geomagnetic activity. During

the course of the year when the Earth's dipole is tilted closer and further from the ecliptic plane in the direction perpendicular to the Earth-Sun line, it can encounter greater and weaker southward interplanetary magnetic fields even though the field is lying in the ecliptic plane. Both the former and latter effects could lead to a semiannual variation of geomagnetic activity because geomagnetic activity is controlled both by the velocity and magnetic field of the solar wind.

We can test how the Earth responds to these two possible effects by using a terrestrial geomagnetic index, designed to represent the level of disturbance of the Earth's magnetosphere. One such suitable index is the am index based on worldwide magnetic records at mid-latitudes. It is linearly related to the size of the magnetic disturbance seen in the magnetogram records and has been normalized to be uniform in Universal Time as the Earth rotates. As shown by the annual variation of the Am index in Figure 25, the latter (magnetic) control is stronger than the former (solar wind velocity) effect, since the top two panels that divide the data according to the direction of the east-west component of the IMF would each show evidence for a semiannual variation in geomagnetic activity if the velocity control were dominant. Rather two annual variations are seen, controlled by IMF direction.

Another effect that could be heliolatitude dependent is one due to the variance of the solar wind velocity. X. Li [this volume] has reported that fast solar wind streams have significantly larger variance in the velocity than slow streams possibly explaining enhanced diffusion and acceleration of MeV electrons in the terrestrial magnetosphere. The source of this variation may be due to the existence of thin jets of high velocity plasma near the base of coronal holes [*Feldman*, 1997].

4. Effects of Solar Rotation

Since the sun rotates, material emitted from the same source region lines up along an Archimedean spiral as illustrated in Figure 26. Since the magnetic field lines passing through those parcels also originate in this source region, the magnetic field too forms an Archimedean spiral pattern that at 1 AU makes an angle of about 45^{o} to the solar radial direction for a 400 km s^{-1} solar wind velocity. Variations in solar wind velocity, and processes acting in the solar wind and corona, including reconnection, create a spread in directions about the average spiral angle as shown above in Figure 19.

If the sun's magnetic axis were aligned with the rotation axis, and the solar magnetic field were axially symmetric, the fast and slow solar wind streams would not interact. However, even at solar minimum when the coronal magnetic structure is simple, the tilt of the streamer belt allows the fast streams to run into the slow streams as shown in Figure 27. This collision compresses the trailing edge of the slow stream and the leading edge of the fast stream. Thus the pattern of solar wind density and speed seen in the solar wind is a combination of a pattern imposed by the magnetic structure of the sun plus the effects of the interaction between streams. Figure 28 shows three solar rotations of data obtained by Mariner 2 in 1962, illustrating the fast-slow stream structure (heavy line) and the density variation (light line) accompanying it. These data, some of the first obtained in the solar wind, illustrate the general anti-correlation of density and velocity of the solar wind illustrated statistically in Figure 7. The structure in these quantities arises principally in their source regions on the sun caused by the magnetic control discussed above. There are kinematic effects as the fronts of the fast streams steepen when the fast core of a stream overtakes the slower leading edge as on October 8, November 15 and November 21. There are also what we term dynamic effects when the fast stream compresses the back end of

the slow stream in front of it. Examples of this effect can be found on October 7, November 14 and November 29. Inside 1 AU the "dynamic" interaction between streams is less important in creating the observed density structure than the structure in the coronal source regions and their kinematic evolution within streams but at greater distances dynamic interactions become quite important.

At times during the solar cycle, especially during the declining phase, the stream structure is quite steady from rotation to rotation. This in turn leads to recurrence in terrestrial geomagnetic activity every time the same fast stream sweeps over the Earth. This is illustrated with the geomagnetic C9 index in Figure 29. The C9 index represents the peak of the early twentieth-century geomagnetician's art in attempting to visualize the effect of the Sun on the terrestrial magnetosphere. The font of the numbers printed illustrates on a logarithmic scale the strength of activity. The R9 column gives the average sunspot number every 3 days for each solar rotation. This is followed by the rotation number and the first day of the solar rotation. Then follows the C9 index for each day of the rotation with a week of overlapping data after the vertical line. The C9 index was only semi-quantitative but still extremely useful as this figure illustrates. The left most column shows the peaking of solar activity in 1971 and 1972 followed by the declining phase in 1973 and 1974. There is little recurrence of geomagnetic activity near solar maximum but at the end of 1973 and throughout 1974 the activity has strong recurrence, certainly associated with two long-lived fast streams.

5. Time Variation

Evidence for century-long changes in the solar wind and interplanetary magnetic field can be obtained from the geomagnetic record [*Russell*, 1975; *Russell and Mulligan*, 1995] and even longer period changes are implied by optical data on sunspots and ^{14}C in tree rings. On

shorter scales the sun has a 22-year magnetic cycle and an 11-year sunspot cycle, and on time scales of less than a day the sun manifests disturbances of the corona called coronal mass ejections (CMEs). When seen head on these CME disturbances may envelop the visible sun as they move directly toward the Earth appearing as "halos" around the sun [*Plunkett et al*., 1998]. When seen above the solar limbs they subtend an angle of about 45^{o} at the sun. Most importantly for Earth these disturbances frequently spawn magnetic clouds travelling through the solar wind, regions of twisted, strong magnetic flux that are very effective at producing geomagnetic activity. The modern paradigm for such a structure is shown in Figure 30 [*Burlaga* 1988; *Lepping et al*., 1990]. The frequent presence of electrons streaming in both directions along the magnetic field suggests that at least some parts of these structures are connected to the Sun. The gradual rotation in the magnetic field seen as these structures pass, suggests that they form twisted magnetic tubes.

The way we characterize such a structure is to invert the magnetic time series to obtain a best-fit model. A recent approach of *Mulligan and Russell* [2000] allows both force free and non-force-free ropes to be fit and it allows the rope to expand. The model obtains the total flux, the current flowing and the orientation of each rope. Most ropes are found to be force-free meaning that the outward pressure in the rope due to the increased magnetic field there is balanced entirely by the inward force due to the curvature of the magnetic field. The pressure in the plasma does not play a significant role.

This observation is consistent with the observation that the plasma pressure in these ropes is much less than the magnetic pressure i.e. they are low beta structures. Occasionally we have contemporaneous observations with multiple spacecraft in the same interplanetary coronal mass ejection or ICME [*Mulligan et al*., 1999; *Mulligan and Russell*, 2000]. An example of the results

of the study of such an interval with two relatively close spacecraft is shown in Figure 31. The assumption that the ropes are cylindrically symmetric here leads to a solution in which two separate but similar ropes are found adjacent to each other. While the cylindrical model requires multiple ropes in this ICME, it is more probable that the cross-section of the rope is oval and that there is but a single rope. In either case we must change our paradigm of a magnetic cloud from that shown in Figure 30. The ICME consists either of multiple flux ropes expanding in a shell or an azimuthally extended oval rope. In either case the radial thickness of the ICME is about 0.2 AU and the major radius of curvature of the ICME is close to an AU as sketched in Figure 31. In order to predict the terrestrial disturbance from an ICME one needs to ensure that one has measured the flux tube that will impact the Earth, is using an appropriate model with which to invert its properties, and has obtained a good and unique inversion. Multiple spacecraft maybe needed for this. The average orientation of the axes of these flux tubes varies during the solar cycle roughly following the heliomagnetic equator [*Mulligan et al*., 1998; *Mulligan et al*., 2000b]. This can affect the nature of the geomagnetic activity associated with the arrival of these ropes. We should emphasize that when the ejecta of a CME travels faster than the ambient solar wind plasma it overtakes the upstream magnetized plasma that then drapes over the structure. If the relative velocity is greater than the magnetosonic Mach number a fast mode shock arises in front of the ejecta.

How does the sun make these ropes? It is possible that the twisting of flux tubes by shearing motions in the photospheric plasma can make ropes. Such velocity shear is thought to be responsible for magnetic flux ropes in the Venus ionosphere [*Russell and Elphic*, 1979; *Elphic and Russell*, 1983 a, b]. The ropes are formed at high altitudes and sink in the flowing ionospheric plasma becoming more twisted. At low altitudes where the twist is the greatest, the

ropes appear to become kink unstable [*Elphic and Russell*, 1983c]. Kinking may also occur on the Sun and be responsible for the observed S-shaped arcades. As sketched in Figure 32 reconnection across the heliospheric current sheet may also be able to make ropes, just like ropes are created in the geomagnetic tail. Such a mechanism was recently proposed by *Moldwin et al*. [2000] to produce small flux ropes seen in the solar wind at 1 AU. It would require reconnection to proceed well into the region of open field lines to produce flux ropes of the size of those observed in ICMEs. In addition it would require the existence of multiple current layers reconnecting simultaneously to produce the multiple flux ropes observed. Finally, it is possible to make flux ropes out of coronal arches by reconnection as shown in Figure 33 [*Gosling*, 1990].

The reason we are interested in interplanetary coronal mass ejections is that they provide the solar wind conditions that lead to the most disturbed geomagnetic conditions. As mentioned in the introduction the energy flow into the magnetosphere is greatest when the interplanetary magnetic field is southward. More precisely it is proportional to the rate at which southward magnetic flux is carried to the magnetosphere by the solar wind [*Burton et al*., 1975]. The relative occurrence of this quantity, VBz, that has units of electric field is shown for ICMEs and stream interfaces in Figure 34 [*Lindsay et al*., 1995]. Thus the occurrence of these structures is controlled by the sunspot cycle and peaks when the sunspots do [*Lindsay et al*., 1994]. While other types of solar wind disturbances have a role in affecting aspects of geomagnetic interaction such as corotating solar wind stream interaction regions and regions of high Alfven wave content, the magnetosphere responds to these smaller disturbances principally at high geomagnetic latitudes. In fact, the buildup of the ring current, a major signature of geomagnetic storms, seems to require strong, long lasting southward IMF over periods of hours [*Russell et al*., 2000]. Short period disturbances with durations less than 20 min. appear to be averaged out by

the magnetosphere [*Burton et al*., 1975].

Concluding Remarks

The key to understanding the heating and acceleration of the solar wind is to determine what mechanisms create the decidedly non-Maxwellian distributions of the electrons and ions. If the high temperatures of the corona can be explained with a theory that uses non-Maxwellian distributions, explicit coronal heating mechanisms such as via waves may be unnecessary, but such a theory relegates the solar wind acceleration problem to what causes these non-Maxwellian distribution. The magnetic field imposes a 3D structure on the solar wind. This allows fast streams to collide with slow streams in corotating interaction regions and helps generate recurrent geomagnetic activity. Interplanetary coronal mass ejections may contain multiple cylindrical magnetic flux ropes that are narrow compared to the overall width of an ICME but they also may be oval in cross section and fewer in number. The solar magnetic field imposes magnetic polarity and orientation rules on these flux ropes. We need to understand much better the source regions of the solar wind and CMEs, and the mechanisms that create the observed solar wind disturbances and the distributions of solar wind particles. The STEREO mission will make a major step in the former direction and Solar Probe in the latter.

Acknowledgments

We gratefully acknowledge the assistance of J. G. Luhmann, J. A. Newbury, and T. Mulligan in the preparation of this review. This work was supported by the National Aeronautics and Space Administration under contract NAS5-00133-6

References

Asbridge, J. R., S. J. Bame and W. C. Feldman, Abundance differences in solar wind double streams, *Solar Phys*., *37*, 451-467, 1974.

Burlaga, L. F., Magnetic clouds and force-free fields with constant alpha, *J. Geophys. Res*., *93*, 7217, 1988.

Burton, R. K., R. L. McPherron and C. T. Russell, An empirical relationship between interplanetary conditions and Dst, *J. Geophys. Res*., *80*, 4204-4214, 1975.

Elphic, R.C., and C.T. Russell, Magnetic flux ropes in the Venus ionosphere: Observations and models, *J. Geophys. Res*., *88*, 58-72, 1983a.

Elphic, R.C., and C.T. Russell, Global characteristics of magnetic flux ropes in the Venus ionosphere, *J. Geophys. Res.*, *88*, 2993-3004, 1983b.

Elphic, R.C., and C.T. Russell, Evidence for helical kink instability in Venus magnetic flux ropes, *Geophys. Res. Lett.*, *10*, 459-462, 1983c.

Fairfield, D. H., and J. D. Scudder, Polar rain: Solar coronal electrons in the Earth's magnetosphere, *J. Geophys. Res*., *90*, 4055, 1985.

Feldman, W. C., Coronal structure inferred from remote sensing observations, in *Robotic Exploration Close to the Sun*, edited by S. R. Habbal, p.9-24, 1997.

Feldman, W. C., J. R. Asbridge, M. D. Montgomery and S. P. Gary, Solar wind electrons, *J. Geophys. Res*., *80*, 4181-4196, 1975.

Gosling, J. T., Coronal mass ejections and magnetic flux ropes in interplanetary space, in *Physics of Magnetic Flux Ropes*, *Geophys. Monogr. Ser.*, Vol. *58*, edited by C. T. Russell, E. R. Priest, and L. C. Lee, pp.343-364, AGU, Washington, DC, 1990.

Gosling, J. T., Physical nature of the low-speed solar wind, in *Robotic Exploration Close to the Sun: Scientific Bases*, 17-24, American Institute of Physics, 1997.

Hundhausen, A. J., An interplanetary view of coronal holas, in *Coronal Holas and High Speed Streams*, edited by J. B. Zirker, 225-319, Colorado Associated University Press, Boulder, 1977.

Hundhausen, A. J., The solar wind, in *Introduction to Space Physics*, edited by M. G. Kivelson and C. T. Russell, 91-128, Cambridge University Press, New York, 1995.

Klein, L. W., K. W. Ogilvie, and L. F. Burlaga, Coulomb collisions in the solar wind, *J. Geophys. Res*., *90*, 7389-7395, 1985.

Lepping, R. P., J. A. Jones, and L. F. Burlaga, Magnetic field structure of interplanetary magnetic clouds at 1 AU, *J. Geophys. Res*., *95*, 11,957-11,965, 1990.

Li, X. L., this volume, 2000.

Lindsay, G. M., C. T. Russell, J. G. Luhmann, and P. Gazis, On the sources of interplanetary shocks at 0.72 AU, *J. Geophys. Res*., *99*, 11-17, 1994.

Lindsay, G. M., C. T. Russell, and J. G. Luhmann, Coronal mass ejection and stream interaction region characteristics and their potential geomagnetic effectiveness, *J. Geophys. Res*., *100*, 16,999-17,013, 1995.

Linker, J. A., Z. Mikic, D. A. Biesecker, R. J. Forsyth, S. E. Gibson, A. J. Lazarus, A. Lecinski, P. Riley, A. Szabo, and B. J. Thompson, Magnetohydrodynamic modeling of the solar corona during whole sun month, *J. Geophys. Res*., *104*, 9809-9830, 1999.

Luhmann, J. G., T-L. Zhang, S. M. Petrinec and C. T. Russell, Solar cycle 21 effects on the interplanetary magnetic field and related parameters at 0.7 and 1.0 AU, *J. Geophys. Res*., *98*, 5559-5572, 1993.

Marsch, E., K-H. Muhlhauser, R. Schwann, H. Rosenbauer, W. Pilipp, and F. M. Neubauer, Solar wind protons: Three dimensional velocity distributions and derived plasma parameter measured between 0.3 and 1.0 AU, *J. Geophys. Res*., *87*, 52-72, 1982.

McComas, D. J., S. J. Bame, B. L. Barraclough, W. C. Feldman, H. O. Funsten, J. T. Gosling, P. Riley, and R. Skoug, Ulysses' return to the slow solar wind, *Geophys. Res. Lett*., *25*, 1-4, 1998.

McPherron, R. L., Magnetospheric dynamics, in *Introduction to Space Physics*, edited by M. G. Kivelson and C. T. Russell, 400-458, Cambridge University Press, New York, 1995.

Meyer-Vernet, N., Large scale structure of planetary environments: The importance of not being Maxwellian, *Planet. Space Sci*., in press, 2000.

Moldwin, M. B., S. Ford, R. Lepping, J. Slavin, and A. Szabo, Small-scale magnetic flux ropes in the solar wind, *Geophys. Res. Lett*., *27*, 57-60, 2000.

Mulligan, T., and C. T. Russell, The multiple flux rope structure of interplanetary coronal mass ejections, *J. Geophys. Res.*, submitted 2000.

Mulligan, T., C. T. Russell and J. G. Luhmann, Solar cycle evolution of the structure of magnetic clouds in the inner heliosphere, *Geophys. Res. Lett*., *25*, 2959-2962, 1998.

Mulligan, T., C. T. Russell, B. A. Anderson, D. Lohr, D. Rust, B. A. Toth, L. J. Zanetti, M. H. Acuna, R. P. Lepping, and J. T. Gosling, Intercomparison of NEAR and Wind interplanetary coronal mass ejection observations, *J. Geophys. Res*., *104*, 28,217-28,223, 1999.

Mulligan, T., C. T. Russell, and D. Elliott, Modeling of the solar cycle variations in magnetic cloud structure observed at PVO, *Geophys. Res. Lett.*, submitted, 2000.

Neugebauer, M., R. J. Forsyth, A. B. Galvin, K. L. Harvey, J. T. Hoeksema, A. J. Lazarus, R. P. Lepping, J. A. Linker, Z. Mikic, J. T. Steinberg, R. von Steiger, Y.-M. Wang, and R. F.

Wimmer-Schweingruber, Spatial structure of the solar wind and comparisons with solar data and models, *J. Geophys. Res*., *103*, 14,587-14,599, 1998.

Newbury, J. A., Plasma heating and thermal transport in the solar wind near 1 AU, Ph.D. Dissertation, Earth and Space Sciences, UCLA, 2000.

Noyes, R. W., *The Sun our Star*, Harvard University Press, Cambridge, Mass, 1982.

Parker, E. N., Dynamics of the interplanetary gas and magnetic fields, *Astrophys. J., 128*, 664-676, 1958.

Petrinec, S. P., P. Song and C. T. Russell, Solar cycle variations in the size and shape of the magnetopause, *J. Geophys. Res*., *96*, 7893-7896, 1991.

Pilipp, W. G., H. Miggenrieder, M. D. Montgomery, K-H. Muhlhausser, H. Rosenbauer, and R. Schwann, Characteristics of electron velocity distribution functions in the solar wind derived from the Helios plasma experiment, *J. Geophys. Res*., *92*, 1103-1118, 1987.

Pizzo, V. J., Interplanetary shocks on the large scale: A retrospective on the last decades' theoretical efforts, in *Collisionless Shocks in the Heliosphere*: *Reviews of Current Research* (edited by B. T. Tsurutani and R. G. Stone), 51-68, Amer. Geophys. Union, Washington D.C., 1985.

Plunkett, S. P., B. J. Thompson, R. A. Howard, D. J. Michels, O. C. St. Cyr, S. J. Tappin, R. Schwenn and P. L. Lumy, LASCO observations of an Earth-directed coronal mass ejection on May 12, 1997, *Geophys. Res. Lett., 25*, 2477-2480, 1998.

Pneumann, G. W., and R. A. Kopp, Gas-magnetic field interactions in the solar corona, *Solar Phys*., *18*, 258, 1971.

Russell, C. T., On the possibility of determining interplanetary and solar parameters from geomagnetic records, *Solar Phys., 42*, 259-269, 1975.

Russell, C.T., and R.C. Elphic, Observation of magnetic flux ropes in the Venus ionosphere, *Nature, 279*, 616-618, 1979.

Russell, C. T., and T. Mulligan, The 22-year variation of geomagnetic activity: Implications for the polar magnetic field of the Sun, *Geophys. Res. Lett., 22*, 3287-3288, 1995.

Russell, C. T., G. Lu, and J. G. Luhmann, Lessons from the ring current injection during the September 24-25, 1998 storm, *Geophys. Res. Lett., 27*, 1371-1374, 2000.

Scudder, J. D., Why all stars should possess circumstellar temperature inversions, *Astrophys. J*., 398, 319-349, 1992.

Snyder, C. W., M. Neugebauer and U. R. Rao, The solar wind velocity and its correlation with cosmic ray variations and with solar and geomagnetic activity, *J. Geophys. Res*., *68*, 6361-6370, 1963.

Thieme, K. M., E. Marsch, and H. Rosenbauer, Estimates of alpha particle heating in the solar wind inside 0.3 AU, *J. Geophys. Res*., *94*, 1973-1976, 1989.

Wang, Y. M., and N. R. Sheeley, Jr., Solar wind speed and coronal flux-tube expansion, *Astrophys. J*., 355, 726, 1990.

Figure Captions

Figure 1. Plasma temperature from the photosphere, through the chromosphere and transition region to the lower corona. Adapted from Noyes [1982].

Figure 2. Theoretically derived speed of the solar wind from an isothermal model for varying coronal temperatures. Adapted from Parker [1958].

Figure 3. Unnormalized energy per charge spectrum of the solar wind ion population at a time when interpenetrating proton and alpha particles are present. These two alpha particles beams have the same velocities along the magnetic field as the two proton beams. Adapted from Asbridge et al., [1974].

Figure 4. Selected two-dimensional solar-wind ion distributions at varying heliocentric radii as measured by the Helios spacecraft. The dashed line shows the projection of the interplanetary magnetic field in the spin plane of the spacecraft. Adapted from Marsch et al. [1982].

Figure 5. Histogram of the solar wind velocity derived from 18 months of ISEE-3 observations. [Adapted from Newbury, 2000]. Quartiles of the velocity are: 348, 397 and 459 km s^{-1}.

Figure 6. Histogram of the logarithm of the solar wind density derived from 18 months of ISEE-3 observations. Quartiles of the density are: 3.2, 5.2 and 8.4 cm^{-3}. Adapted from Newbury [2000].

Figure 7. The variation of the solar wind density with solar wind velocity. The median, quartiles and mean values are shown. Adapted from Newbury [2000].

Figure 8. The variation of the solar wind proton temperature with the solar wind velocity. The median and quartiles are shown. Adapted from Newbury [2000].

Figure 9. The distribution function of solar wind electrons along the magnetic field direction showing the core and halo populations and their differing bulk velocities and temperatures. Adapted from Feldman et al. [1975].

Figure 10. Typical two-dimensional distribution functions of solar wind electrons showing cuts through the distribution function along the magnetic field. On the left is a distribution with a

noticeable strahl component along the magnetic field. On the right is a distribution that is almost isotropic and having a very weak halo component. Adapted from Pilipp et al. [1987].

Figure 11. The temperature of solar wind electrons as a function of the solar wind velocity. The median and quartiles are shown. Adapted from Newbury [2000].

Figure 12. The temperature of solar wind electrons versus solar wind ion temperature observed by ISEE 3. Individual 5-minute observations are shown. Adapted from Newbury [2000].

Figure 13. Velocity filtration of non-Maxwellian distributions by an attractive force. When the Maxwellian distribution on the lower left moves upward in Z against the force of the attractive potential it loses potential energy, W, and translates to the left, but maintains its slope. The Lorentzian distribution on the right changes its slope when it moves to higher altitude Z and loses potential energy W. [Meyer-Vernet, 2000].

Figure 14. Electron and ion temperatures for solar coronal model using non-Maxwellian distributions and no heat deposition in the coronal [Scudder, 1992].

Figure 15. Phase space density of polar rain versus energy for days with differing solar wind conditions. Adapted from Fairfield and Scudder [1985].

Figure 16. Coronal magnetic field in the Pneumann and Kopp [1971] isothermal solar wind solution. Dashed field lines show the magnetic field lines of a dipole for comparison.

Figure 17. Idealized three dimensional view of the streamer belt and the coronal magnetic field. Orbit of the Earth carries it above and below the sun's equator in the course of the year. Because the streamer belt is tilted with respect to the rotational equator the streamer belt can sweep across the Earth twice every solar rotation. Adapted from Hundhausen [1977].

Figure 18. Sector structure plots for 0.7 AU (bottom) and 1.0 AU (top) showing periods when toward (stippled) and away (solid) magnetic fields were seen by Pioneer Venus and IMP-8. Gaps occur when the spacecraft are in the magnetosheath [Luhmann et al., 1993].

Figure 19. Histograms of the occurrence of various spiral angles in the Pioneer Venus 10-minute averages and the IMP-8 5-minute averages separated according to solar activity level [Luhmann et al., 1993].

Figure 20. Histograms of the occurrence of field magnitudes in the Pioneer Venus 10-minute data and the IMP-8 5-minute data, separated by solar activity level. [Luhmann et al., 1993].

Figure 21. Histograms of the radial or Bx component of the interplanetary magnetic field at IMP-8 and Pioneer Venus for three levels of solar activity. The size of the plot of the IMP-8 data has been scaled to 0.72 AU by a r^{-2} factor to make the plots easily comparable. The dashed vertical lines indicate that the IMP-8 data have a maximum value of 32 nT. [Luhmann et al., 1993].

Figure 22. Histograms of the azimuthal or By component of the interplanetary magnetic field. The size of the plots of the IMP-8 values has been scaled to 0.72 AU by a r^{-1} factor. Other comments of the caption of Figure 21 apply. [Luhmann et al., 1993].

Figure 23. Histograms of the north-south or Bz component of the interplanetary magnetic field. The size of the plots of the IMP-8 values has been scaled to 0.72 AU by a r^{-1} factor. Other comments of the caption of Figure 21 apply. [Luhmann et al., 1993].

Figure 24. More realistic sketch of the structure of the corona and its presumed magnetic field. Adapted from Hundhausen [1995].

Figure 25. The annual variation of the Am index for positive and negative GSM Y component of the interplanetary magnetic field and the difference between the two variations. This illustrates that the magnetic field and not the solar wind velocity is dominantly responsible for the semi-annual variation of geomagnetic activity. [Russell, 1989].

Figure 26. The creation of a spiral magnetic field pattern by the emission of magnetized plasma from a source on the rotating solar surface. Adapted from Hundhausen [1995].

Figure 27. The collision of a fast stream with a slow stream to produce a corotating interaction. Adapted from Pizzo [1985].

Figure 28. Solar wind velocity (dark line) and density (light line) measured by Mariner 2 on three successive solar rotations. Adapted from Hundhausen [1995].

Figure 29. C9 index from 1971 through 1973 showing recurrent geomagnetic activity. Each line corresponds to one solar rotation. [McPherron, 1995].

Figure 30. Modern paradigm of a magnetic cloud often found in ICMEs.

Figure 31. Geometry of the ICME boundary and the two magnetic ropes seen by PVO and ISEE 3 on August 27, 28, 1978. [Mulligan et al., 2000].

Figure 32. Possible method of forming flux ropes by reconnection across the heliospheric current sheet.

Figure 33. Proposed mechanism for creating interplanetary magnetic ropes from arcades in the lower corona. [Gosling, 1990].

Figure 34. Occurrence rate of different values of the east-west interplanetary electric field in ICMEs (top panel), and corotating interaction regions (bottom panel) contrasted with that in the quiet solar wind [Lindsay et al., 1995].

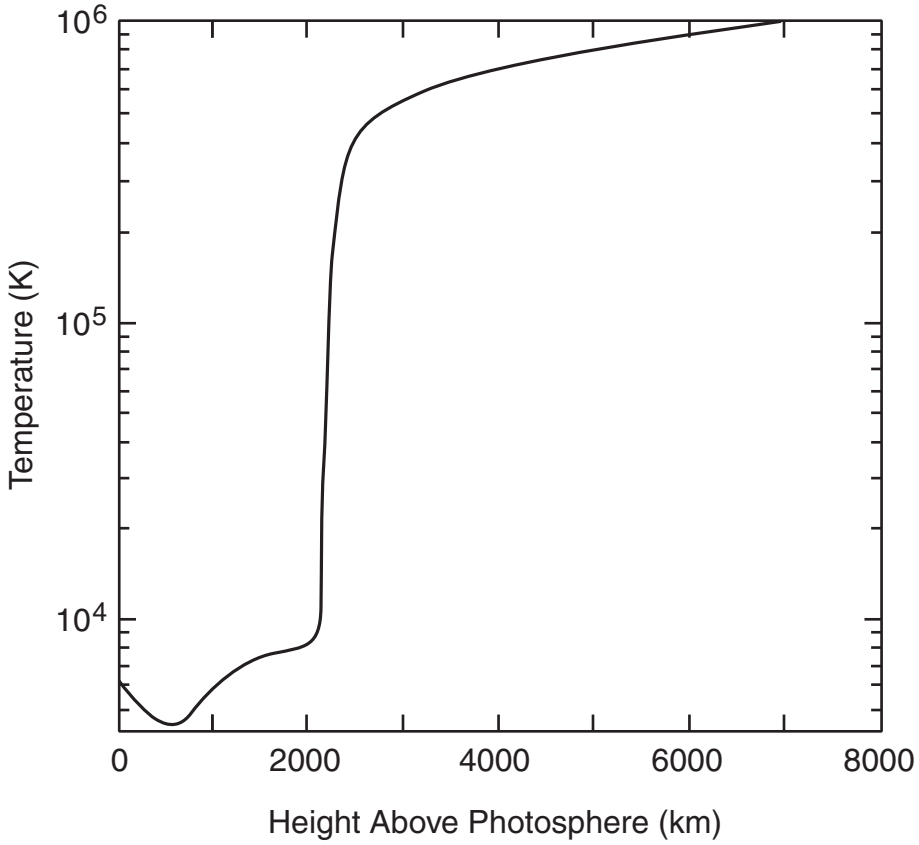
10^6
10^5
10^4
Temperature (K)
0
2000
4000
6000
8000
Height Above Photosphere (km)

Figure 1

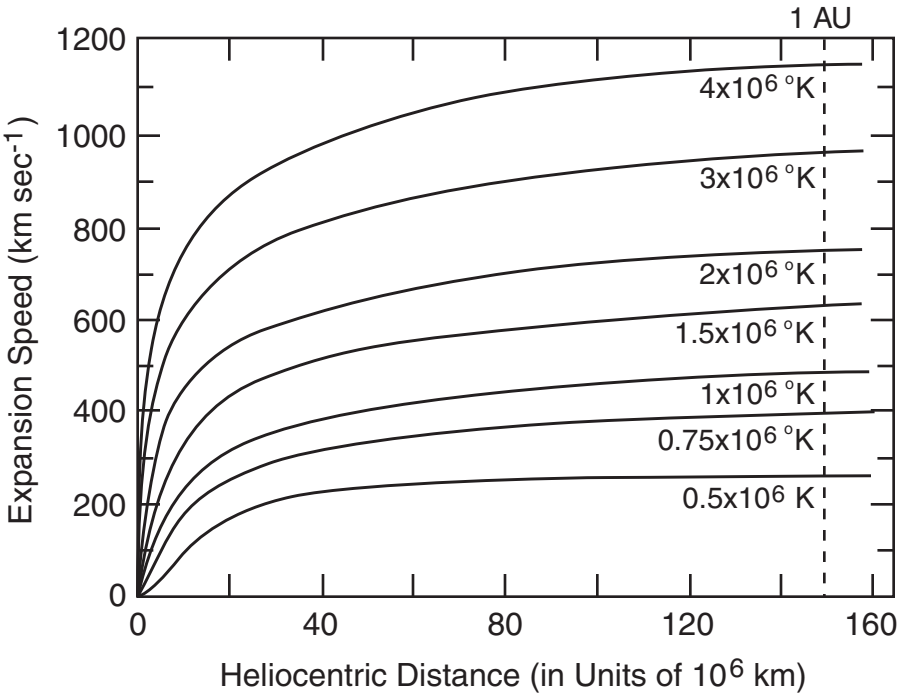
1 AU
1200
1000
800
600
400
200
0
Expansion Speed (km sec-1)
4x10^6 °K
3x10^6 °K
2x10^6 °K
1.5x10^6 °K
1x10^6 °K
0.75x10^6 °K
0.5x10^6 K
0
40
80
120
160
Heliocentric Distance (in Units of 10^6 km)

Figure 2

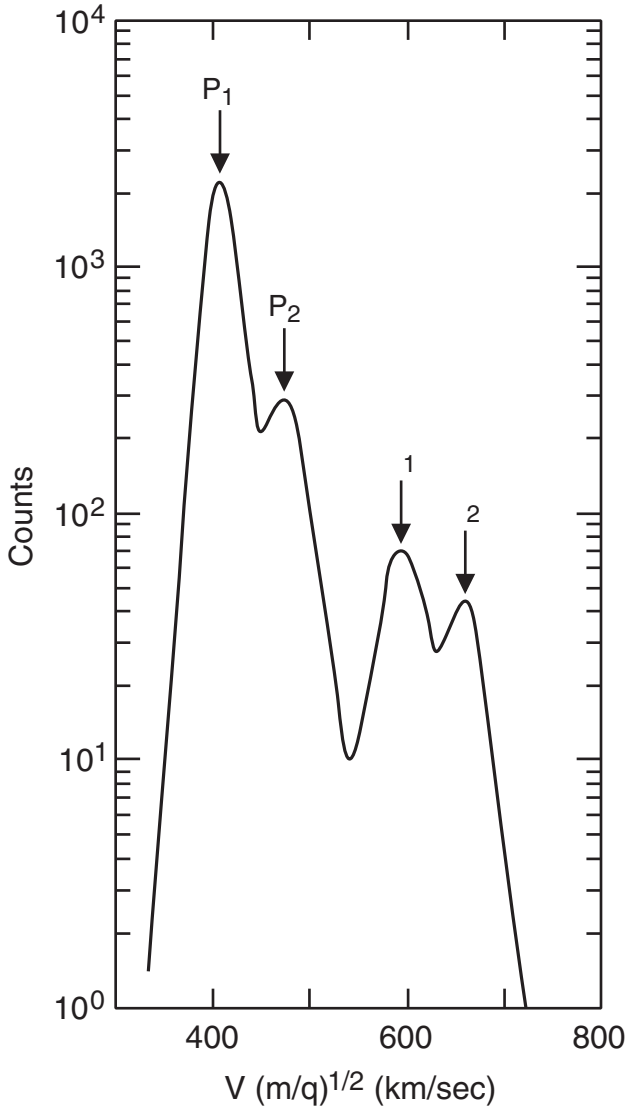

Figure 3

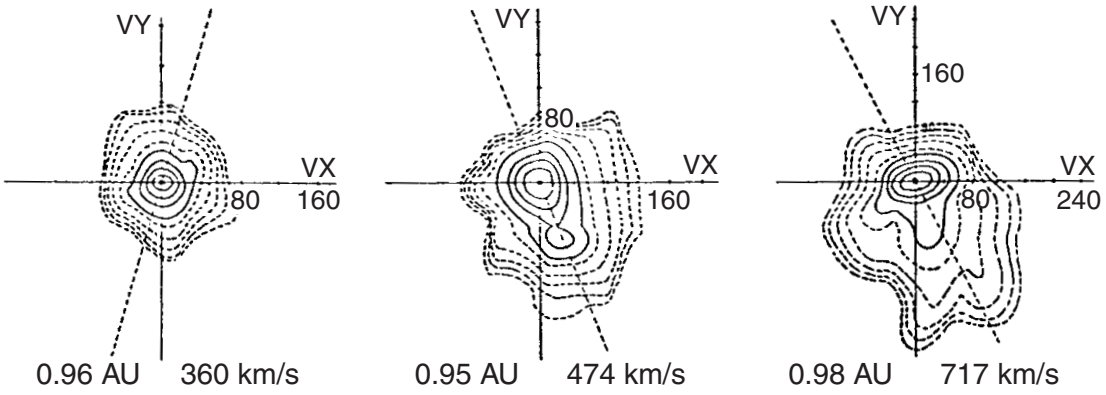
VY
VX
80
160
0.96 AU
360 km/s
VY
80
VX
160
0.95 AU
474 km/s
VY
160
VX
80
240
0.98 AU
717 km/s

Figure 4

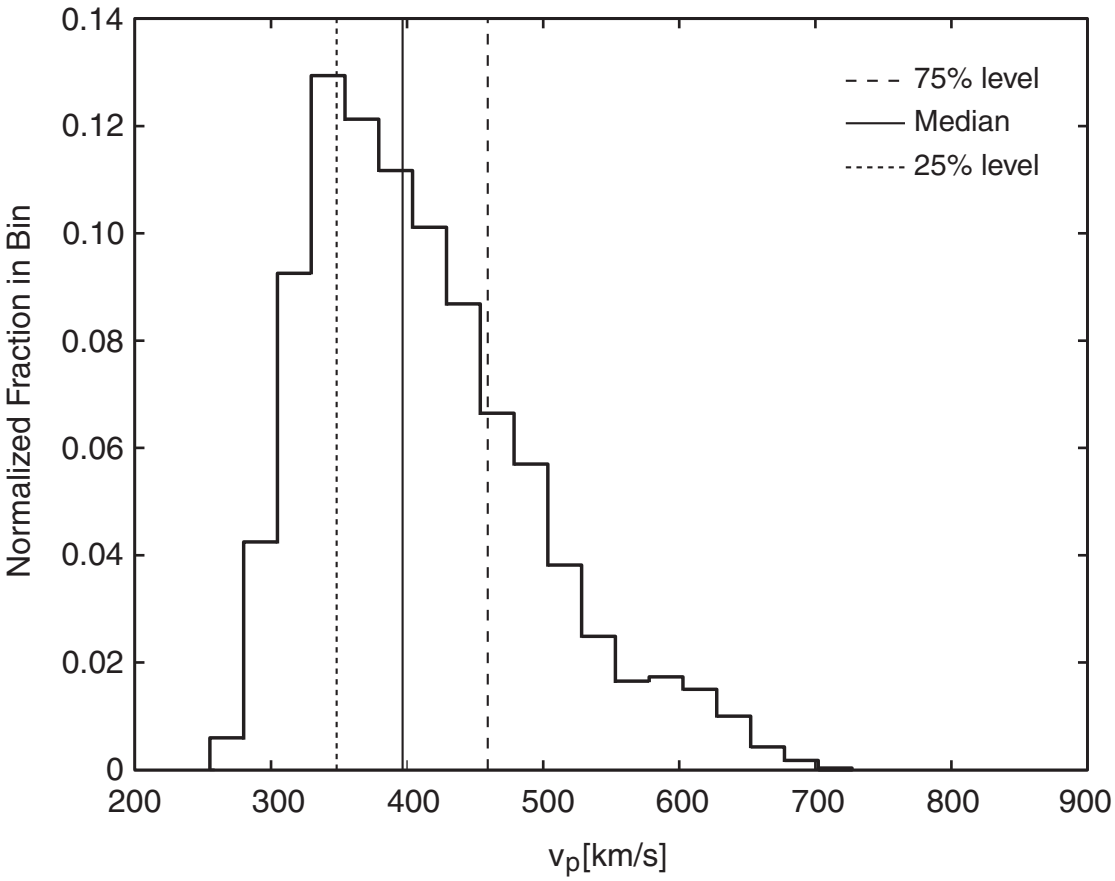
0.14
0.12
0.10
0.08
0.06
0.04
0.02
0
200
300
400
500
600
700
800
900
Normalized Fraction in Bin
v_p[km/s]
75% level
Median
25% level

Figure 5

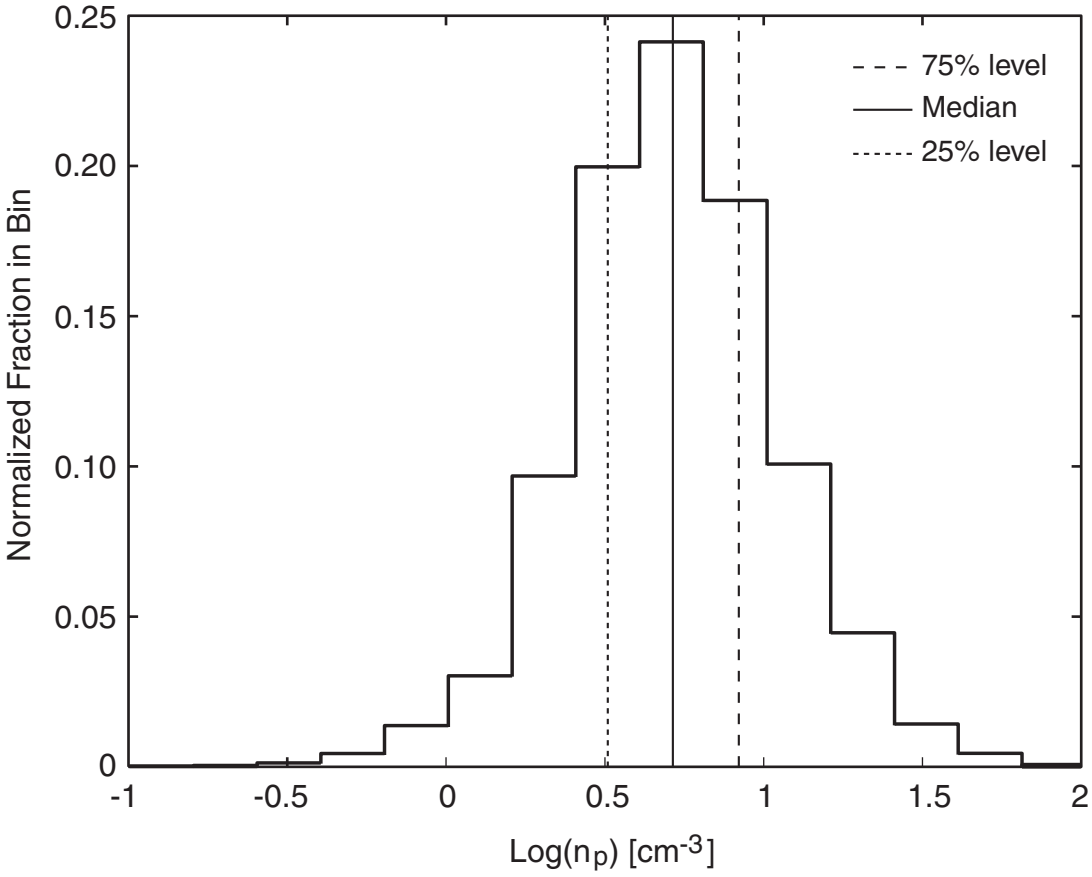
0.25
0.20
0.15
0.10
0.05
0
-1
-0.5
0
0.5
1
1.5
2
Normalized Fraction in Bin
Log(n_p) [cm^-3]
75% level
Median
25% level

Figure 6

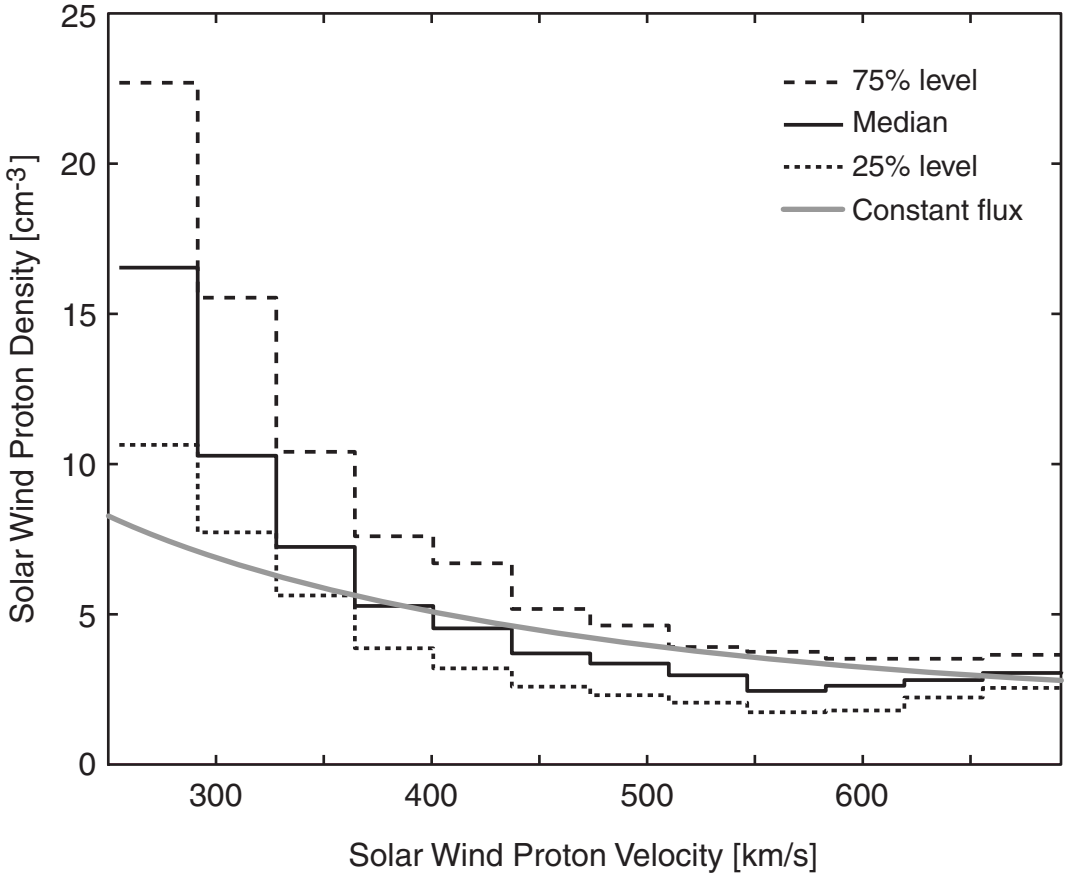
25
20
15
10
5
0
300
400
500
600
Solar Wind Proton Density [cm-3]
Solar Wind Proton Velocity [km/s]
75% level
Median
25% level
Constant flux

Figure 7

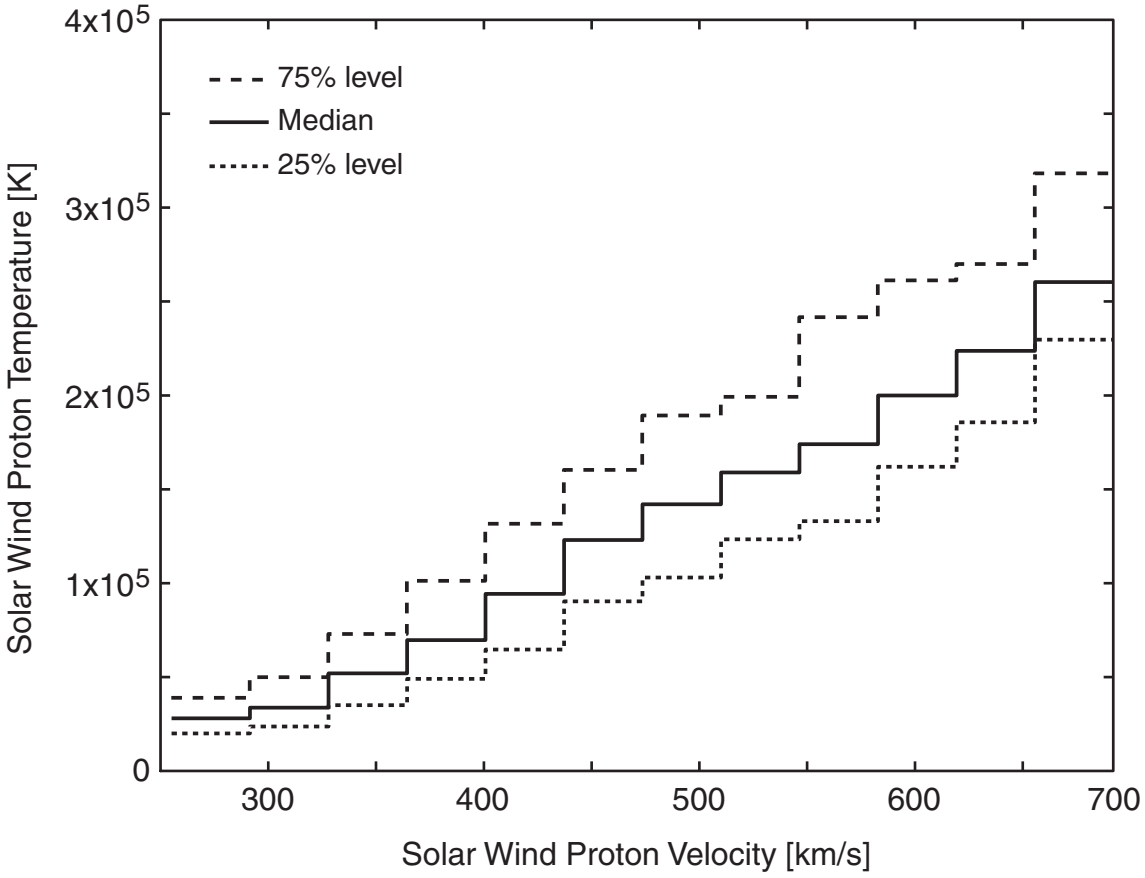
4x10^5
3x10^5
2x10^5
1x10^5
0
75% level
Median
25% level
Solar Wind Proton Temperature [K]
300
400
500
600
700
Solar Wind Proton Velocity [km/s]

Figure 8

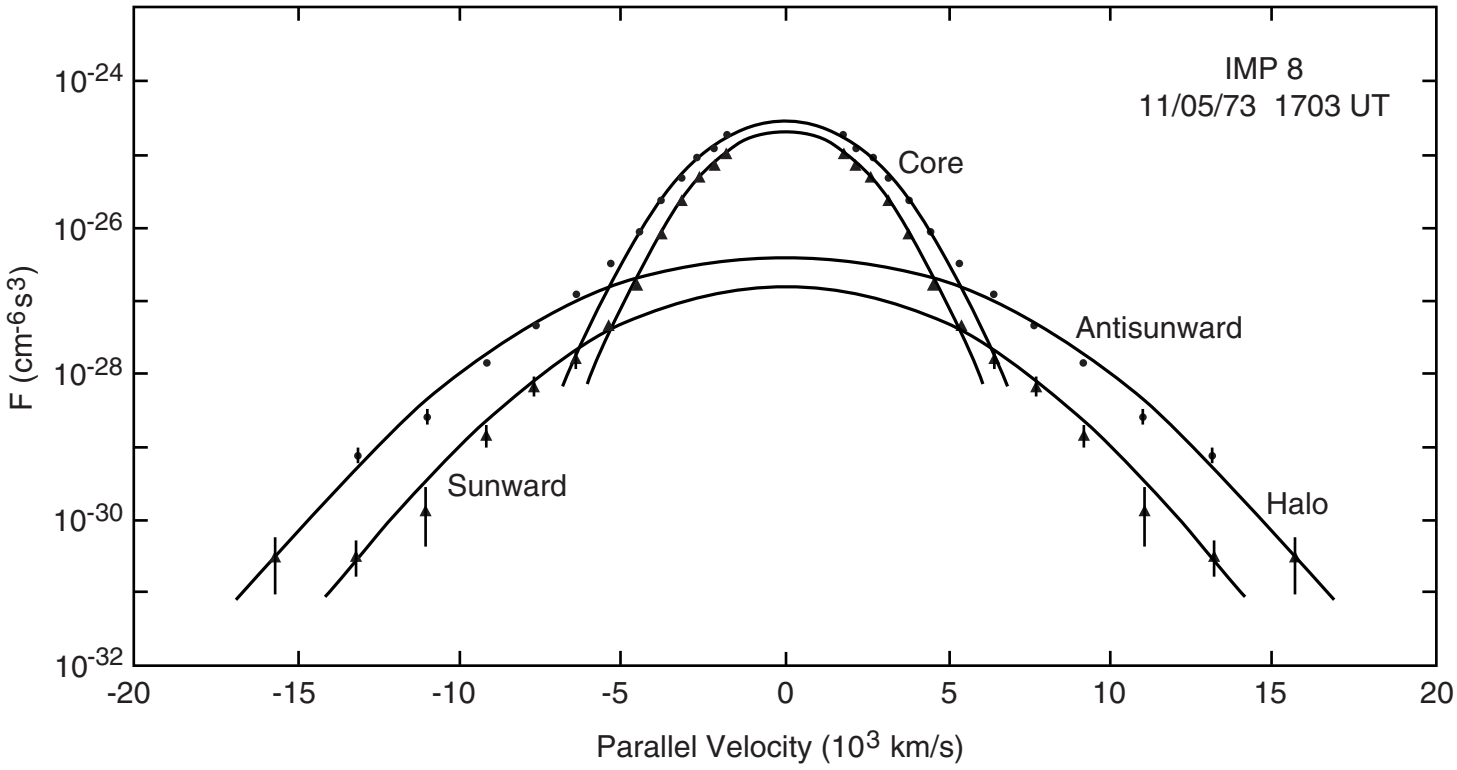
IMP 8
11/05/73 1703 UT
Core
Antisunward
Sunward
Halo
F (cm-6s3)
10-24
10-26
10-28
10-30
10-32
-20
-15
-10
-5
0
5
10
15
20
Parallel Velocity (10^3 km/s)

Figure 9

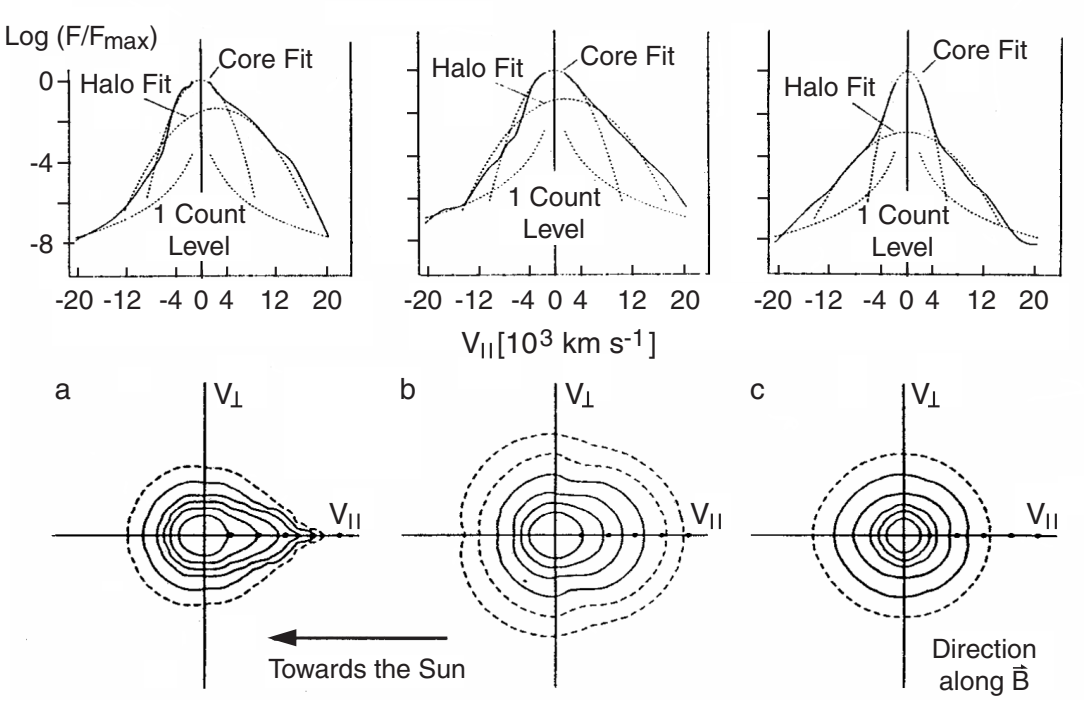
Log (F/Fmax)
0
-4
-8
Halo Fit
Core Fit
1 Count Level
-20 -12 -4 0 4 12 20
VII[10³ km s⁻¹]
a
b
c
V⊥
VII
Towards the Sun
Direction along B

Figure 10

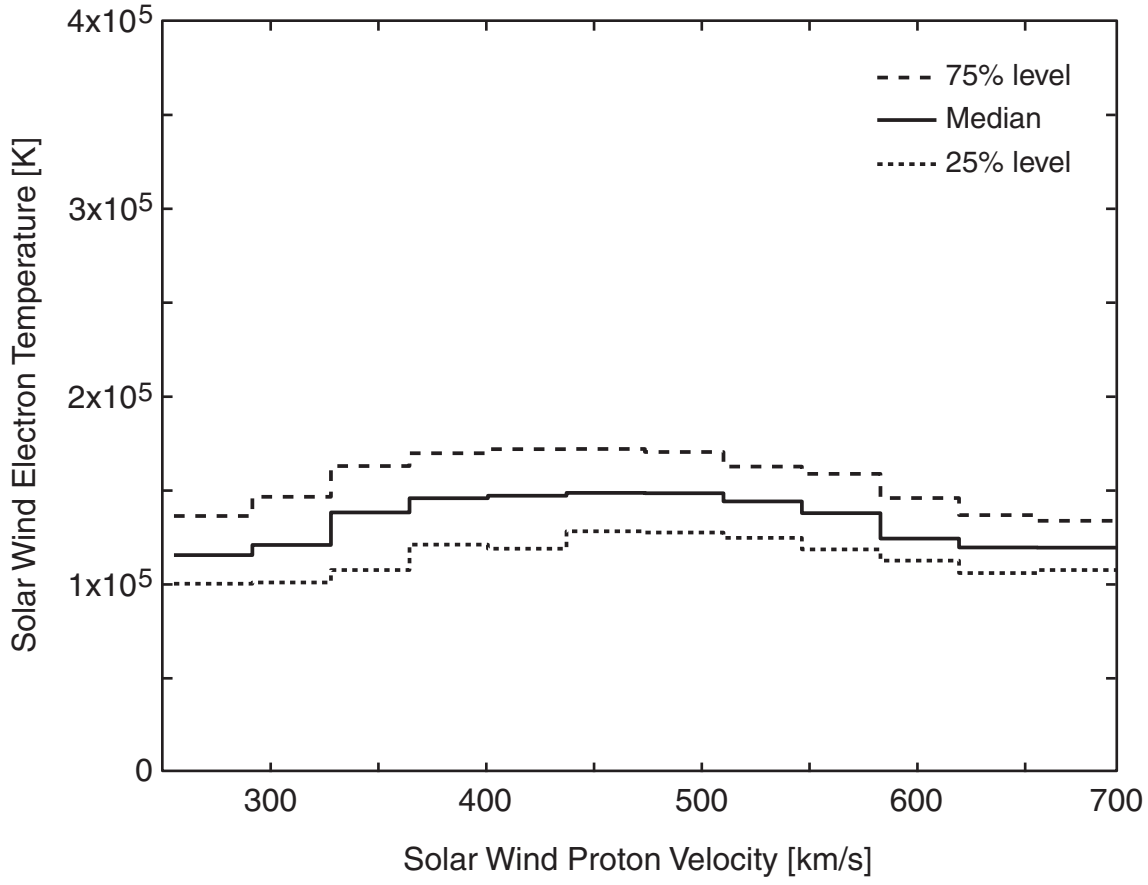
4x10^5
3x10^5
2x10^5
1x10^5
0
Solar Wind Electron Temperature [K]
300
400
500
600
700
Solar Wind Proton Velocity [km/s]
75% level
Median
25% level

Figure 11

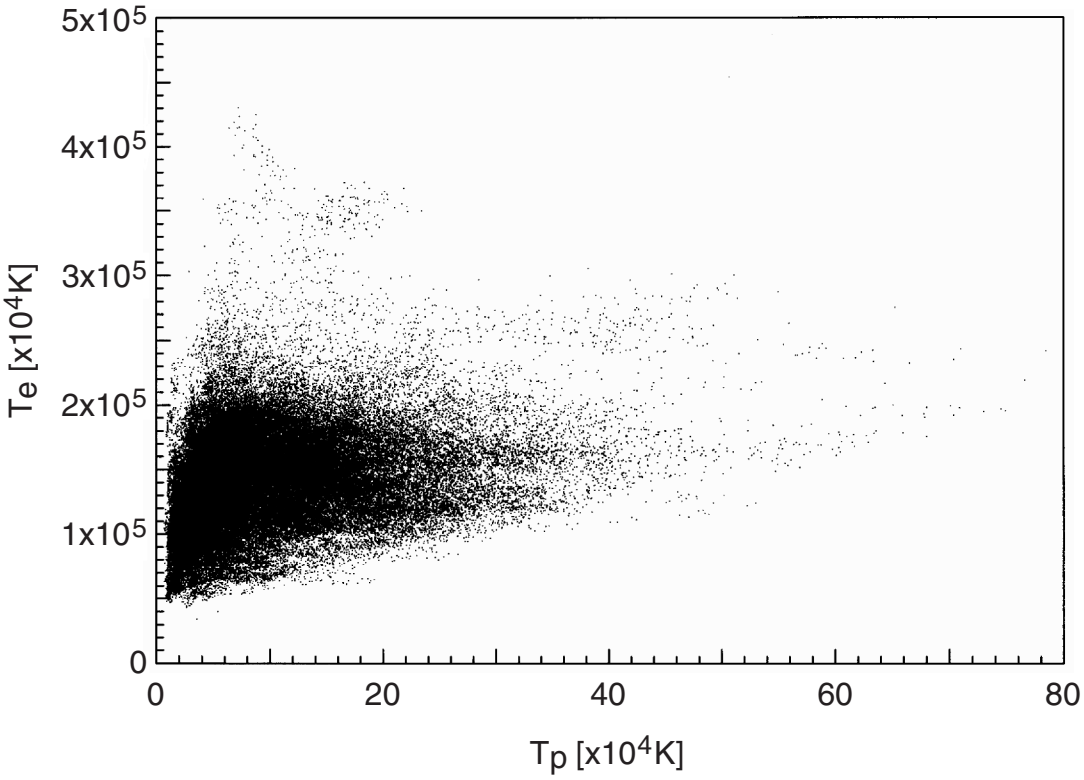

Figure 12

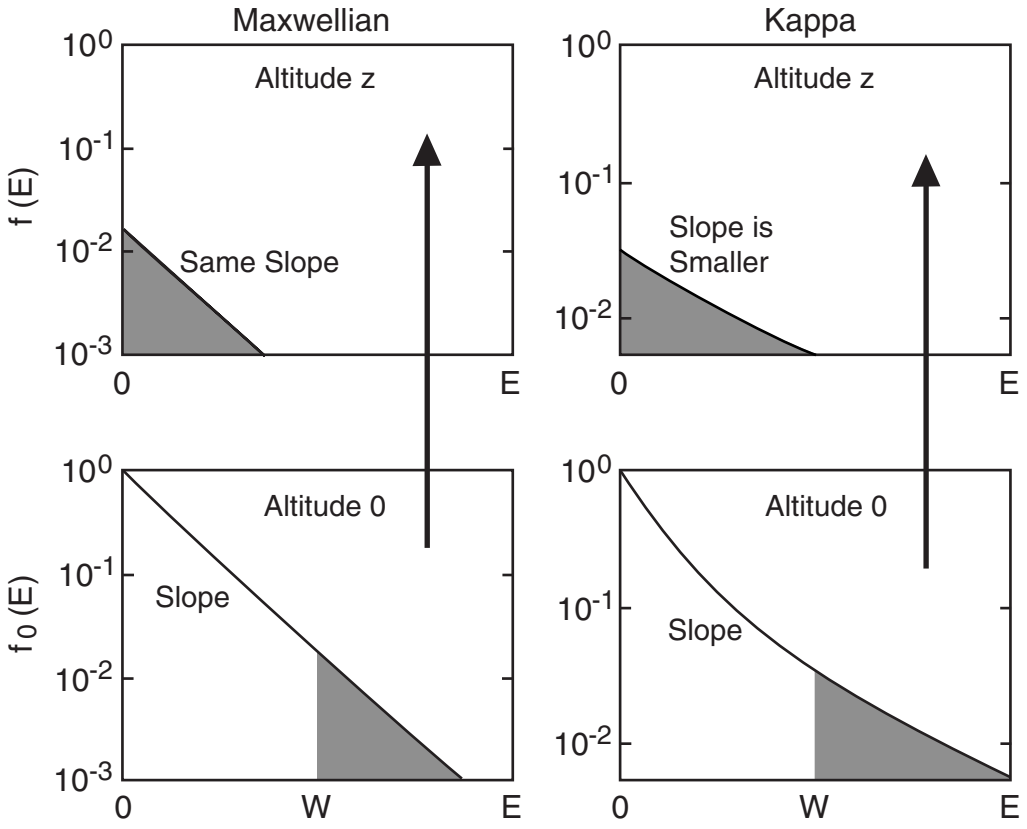
Maxwellian
Kappa
Altitude z
Altitude z
Same Slope
Slope is
Smaller
Altitude 0
Altitude 0
Slope
Slope
f (E)
f0 (E)
10^0
10^-1
10^-2
10^-3
0
W
E

Figure 13

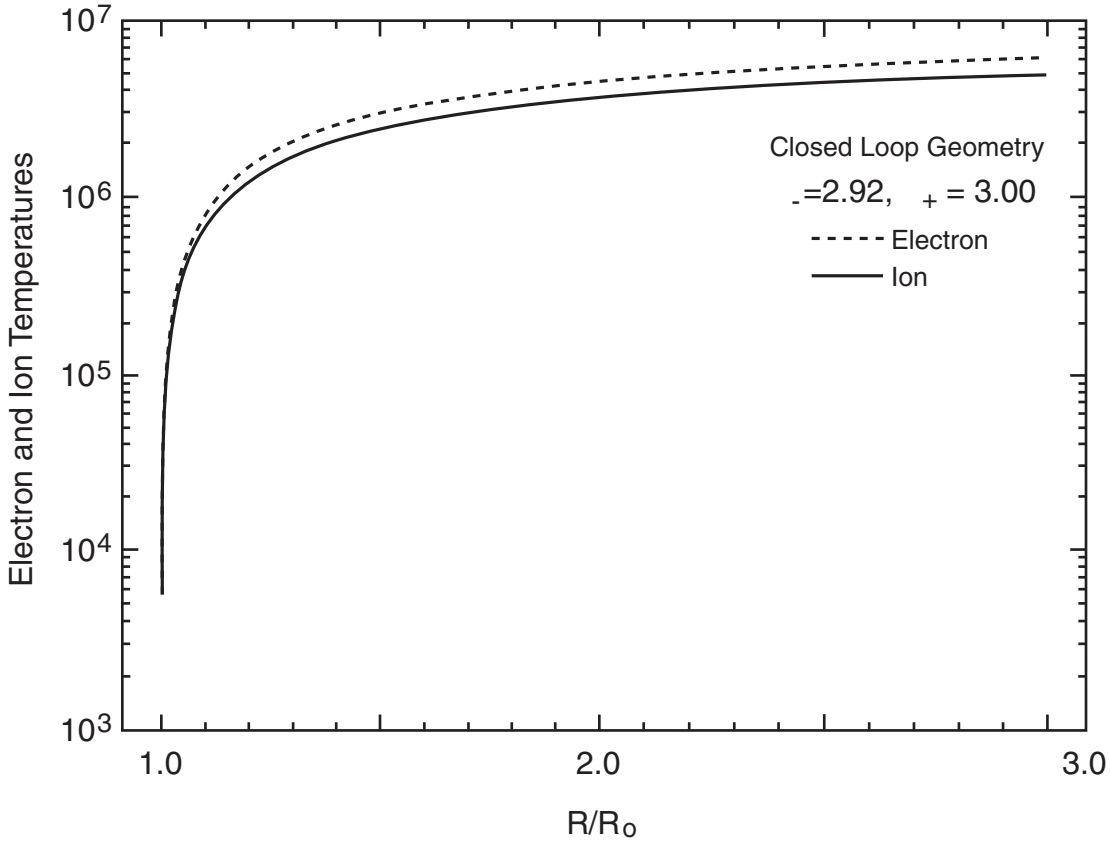
Electron and Ion Temperatures
10^7
10^6
10^5
10^4
10^3
1.0
2.0
3.0
R/R$_o$
Closed Loop Geometry
$_-$=2.92, $_+$ = 3.00
Electron
Ion

Figure 14

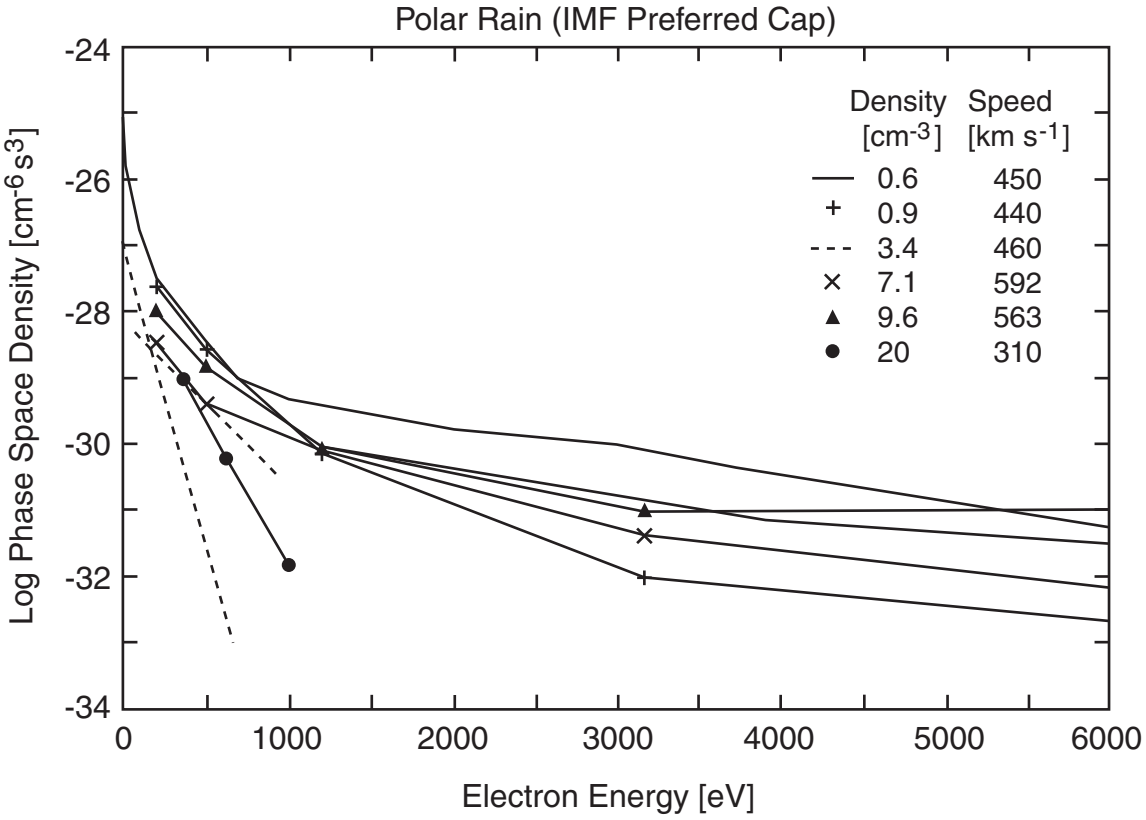
Polar Rain (IMF Preferred Cap)
Log Phase Space Density [cm-6s3]
Electron Energy [eV]
-24
-26
-28
-30
-32
-34
0
1000
2000
3000
4000
5000
6000
Density [cm-3]
Speed [km s-1]
0.6 450
0.9 440
3.4 460
7.1 592
9.6 563
20 310

Figure 15

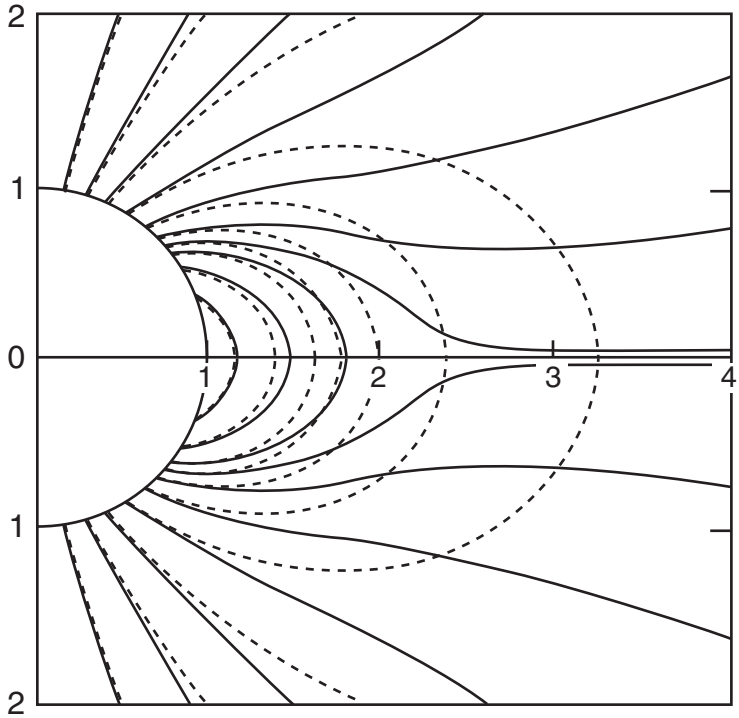

Figure 16

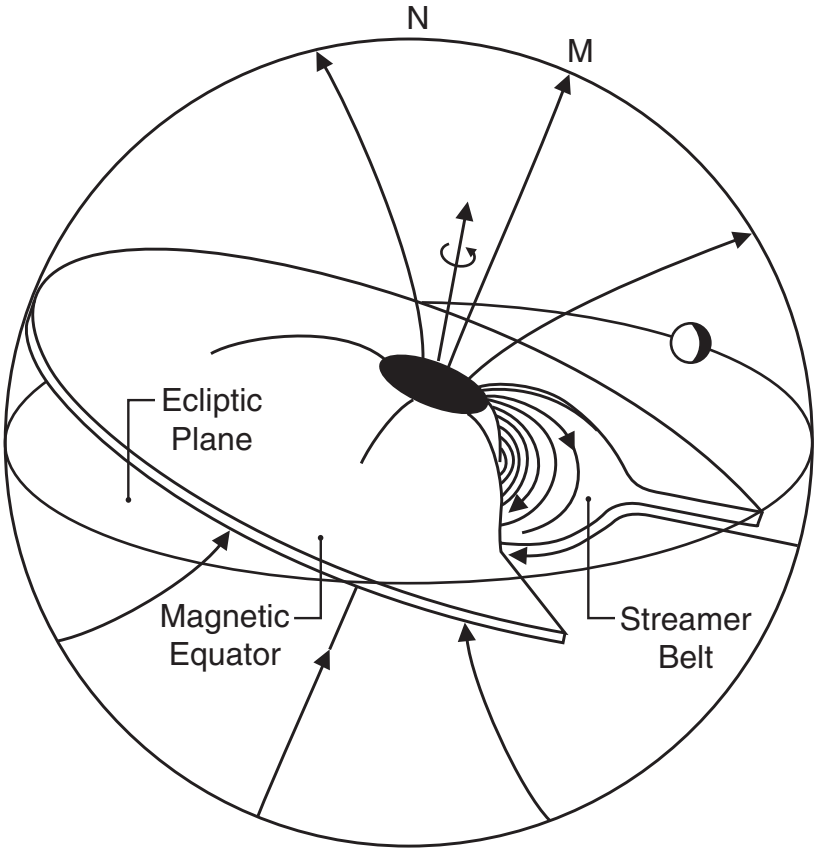

Figure 17

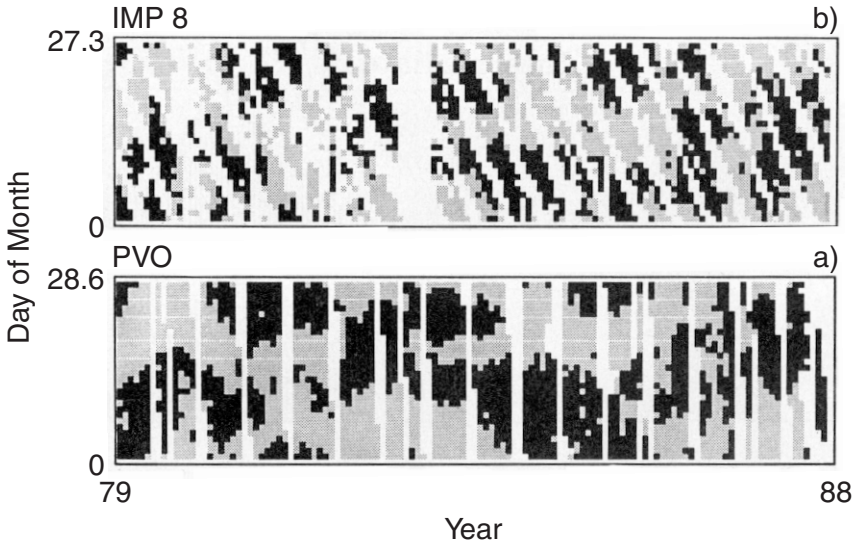

Figure 18

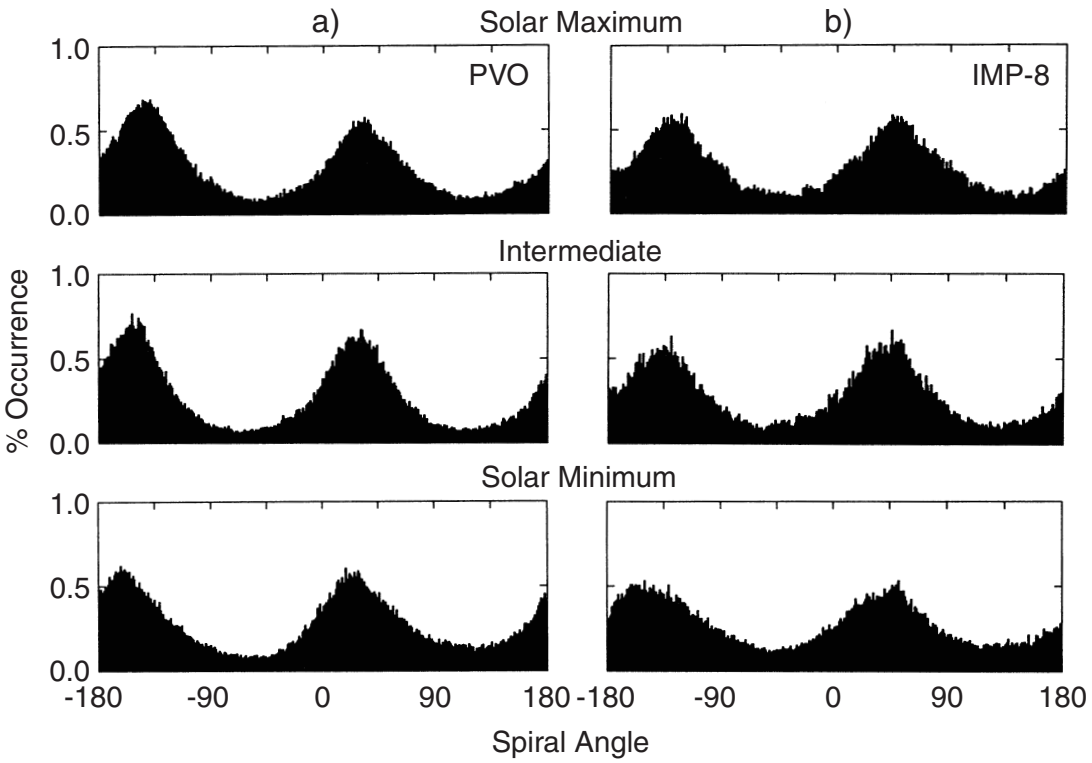
a)
Solar Maximum
b)
PVO
IMP-8
1.0
0.5
0.0
Intermediate
% Occurrence
Solar Minimum
-180
-90
0
90
180
Spiral Angle

Figure 19

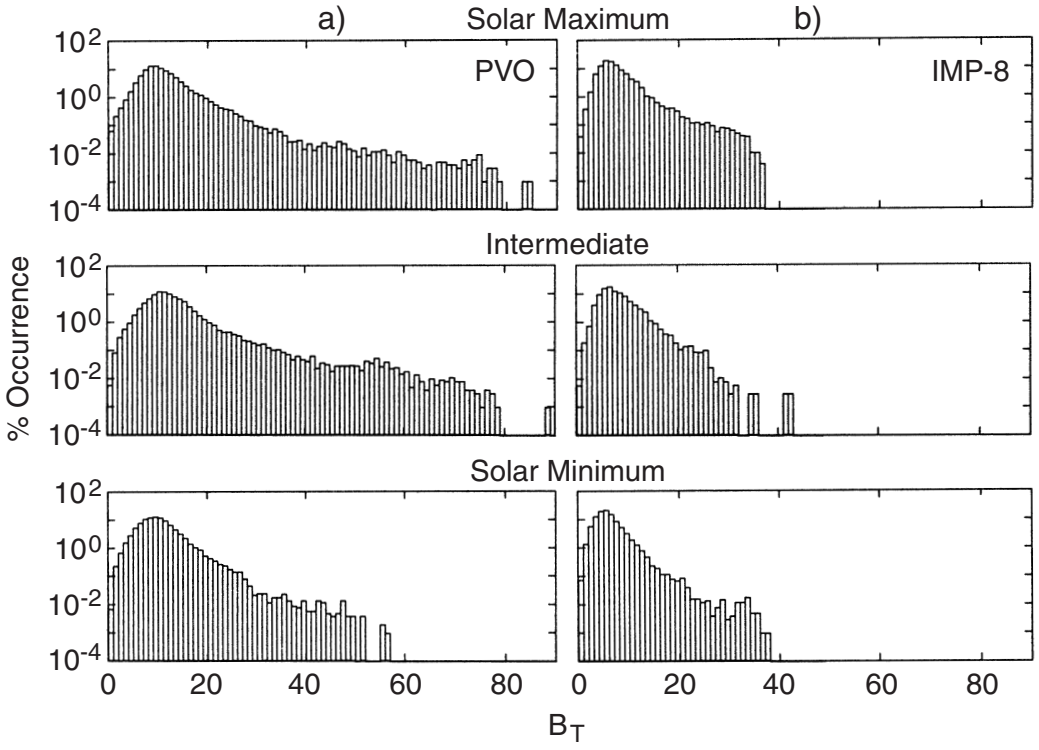
a)
Solar Maximum
b)
PVO
IMP-8
Intermediate
Solar Minimum
% Occurrence
10^2
10^0
10^{-2}
10^{-4}
0
20
40
60
80
B_T

Figure 20

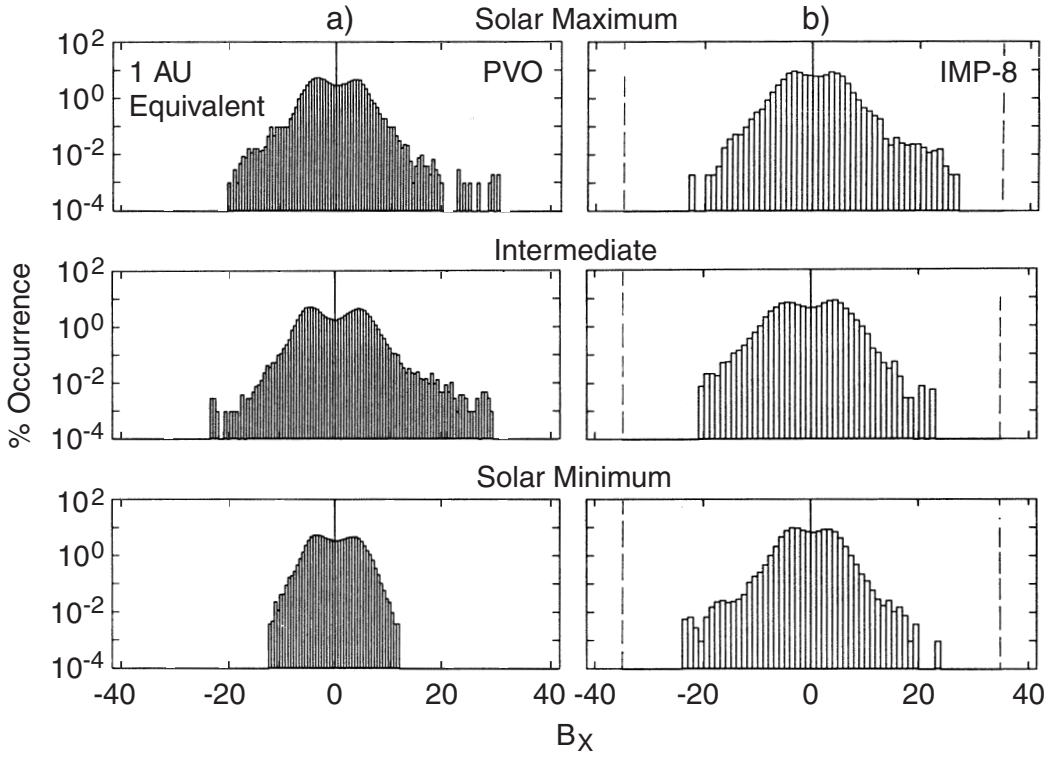
a)
Solar Maximum
b)
1 AU
Equivalent
PVO
IMP-8
Intermediate
Solar Minimum
% Occurrence
10^2
10^0
10^{-2}
10^{-4}
-40
-20
0
20
40
B_X

Figure 21

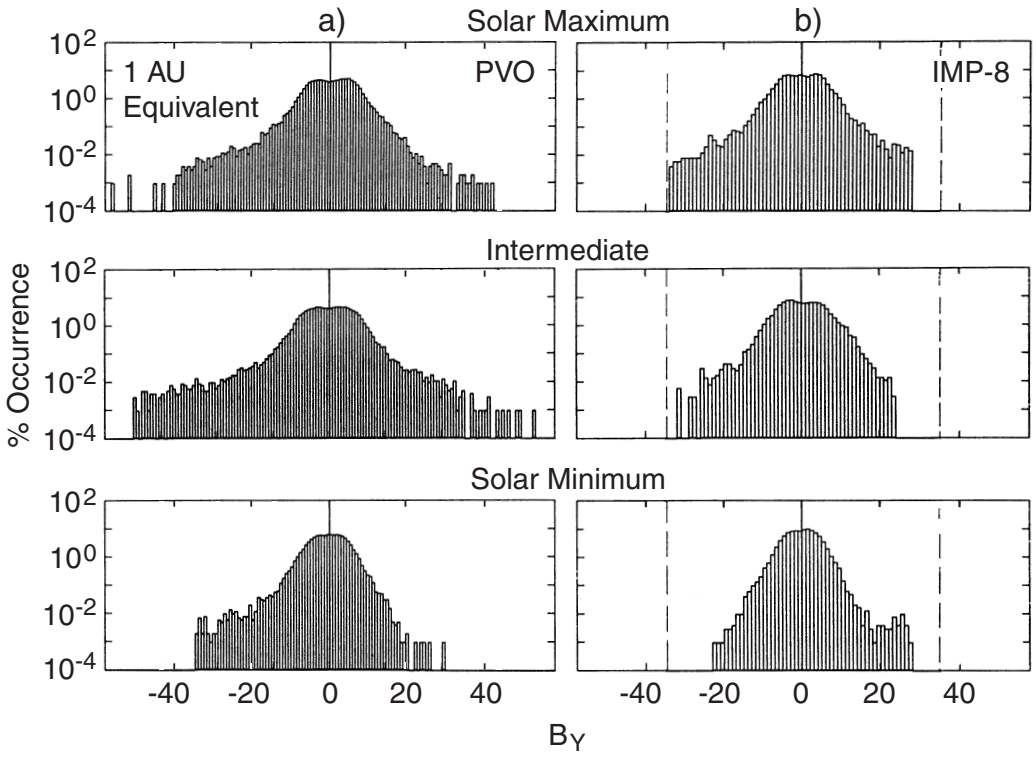
a)
Solar Maximum
b)
1 AU
Equivalent
PVO
IMP-8
Intermediate
Solar Minimum
% Occurrence
10^2
10^0
10^{-2}
10^{-4}
-40
-20
0
20
40
B_Y

Figure 22

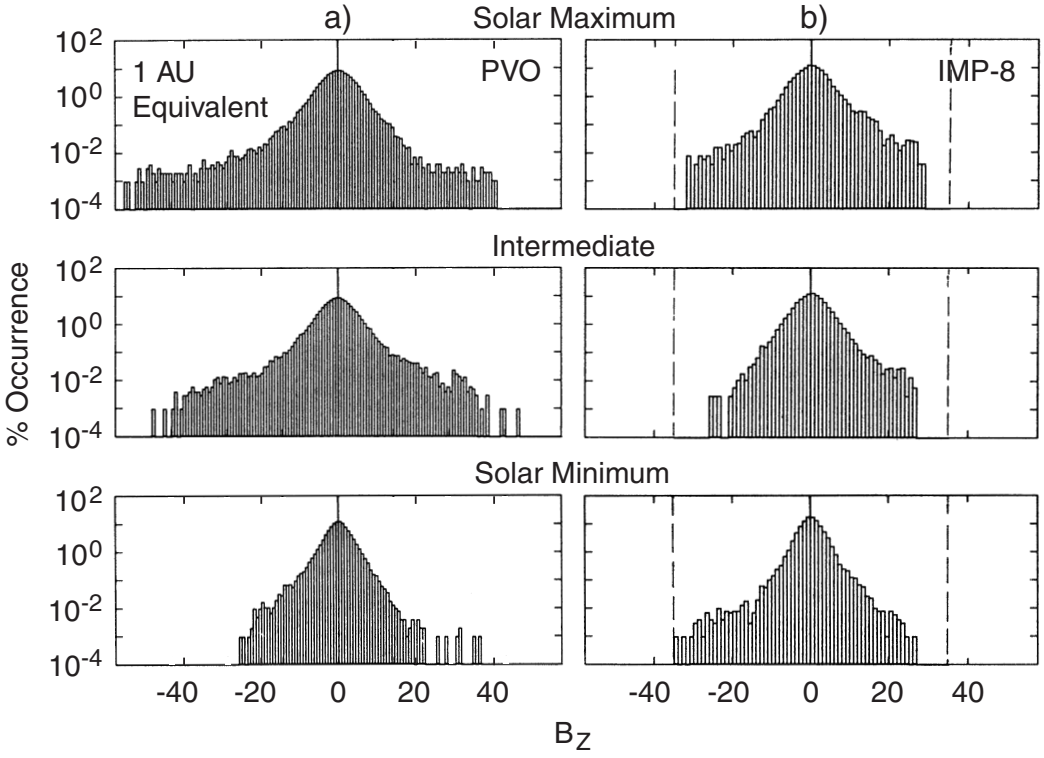
a)
Solar Maximum
b)
1 AU
Equivalent
PVO
IMP-8
Intermediate
Solar Minimum
% Occurrence
10^2
10^0
10^{-2}
10^{-4}
-40
-20
0
20
40
B_Z

Figure 23

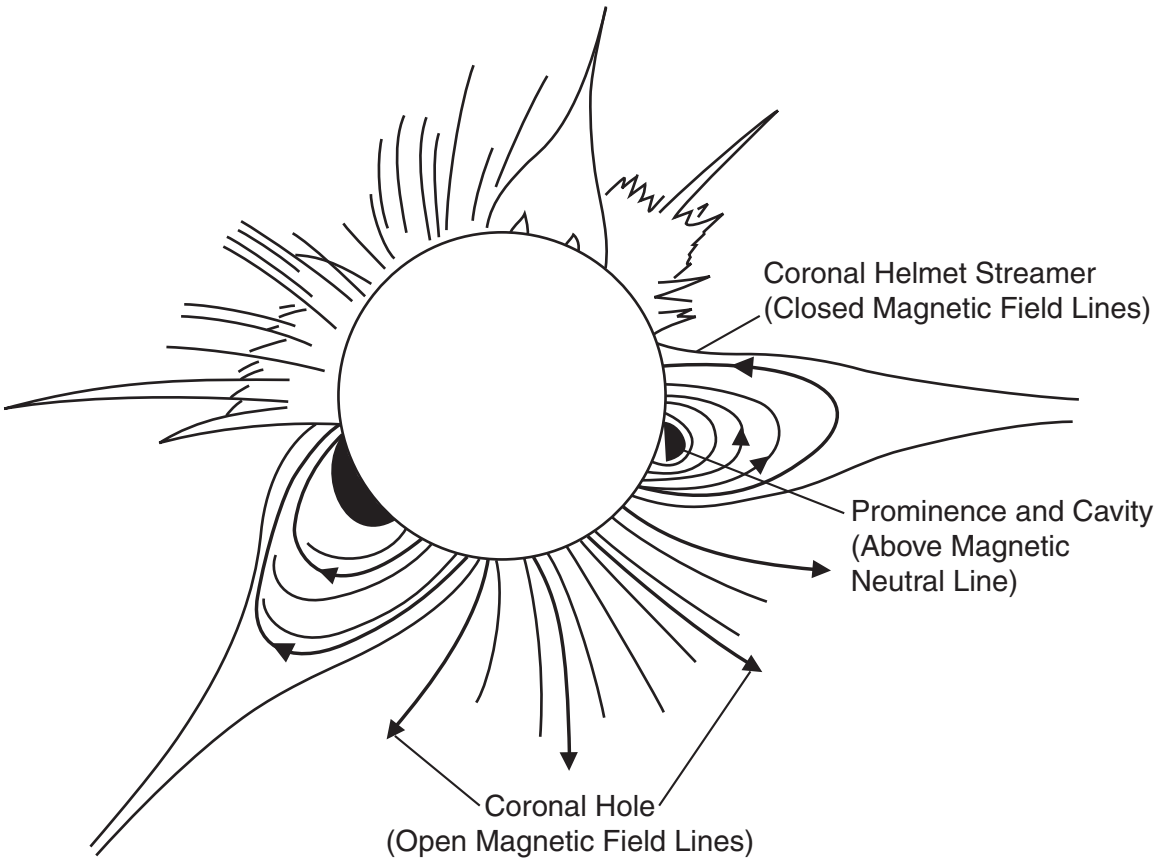
Coronal Helmet Streamer
(Closed Magnetic Field Lines)
Prominence and Cavity
(Above Magnetic
Neutral Line)
Coronal Hole
(Open Magnetic Field Lines)

Figure 24

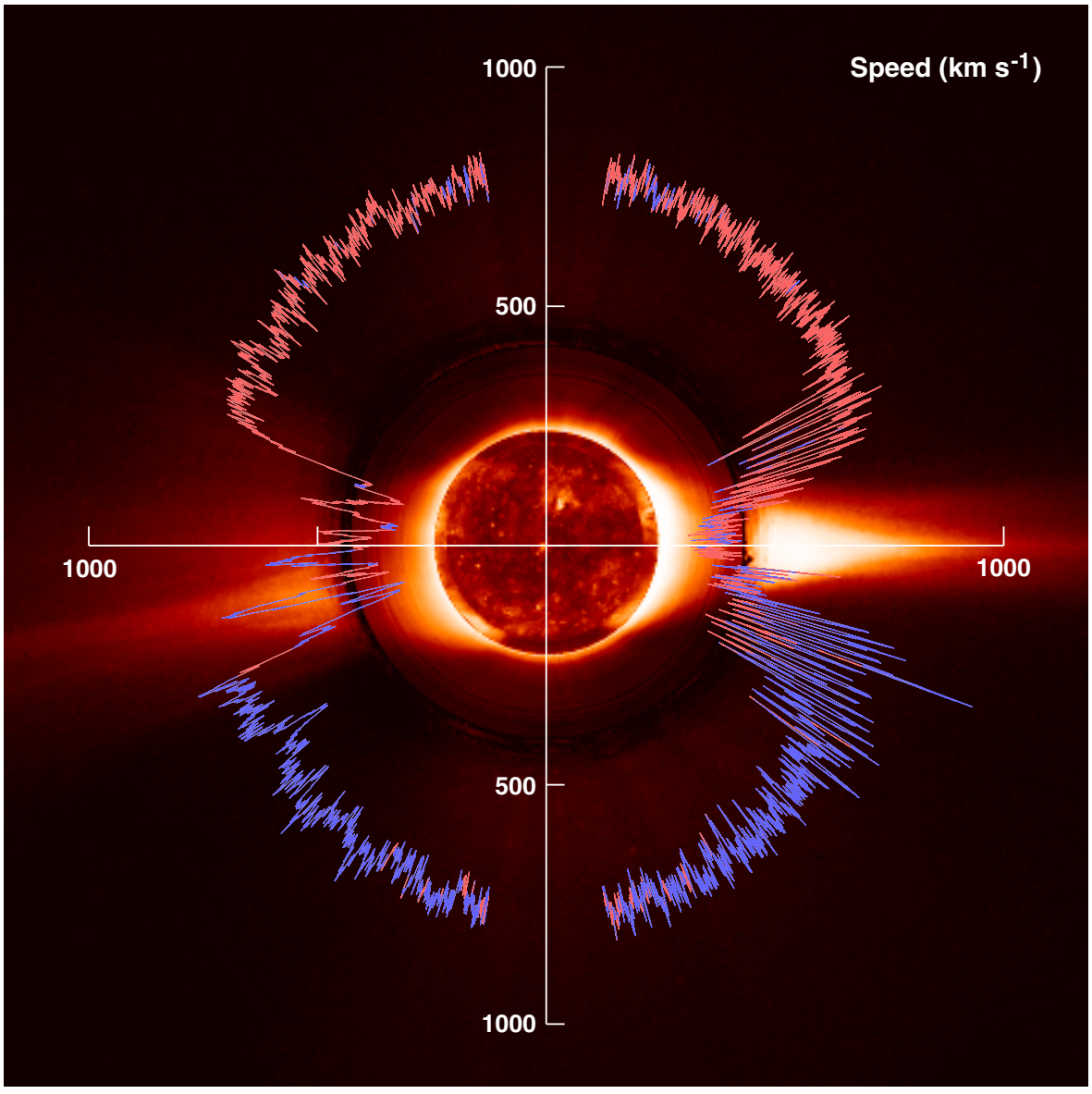

Figure 25

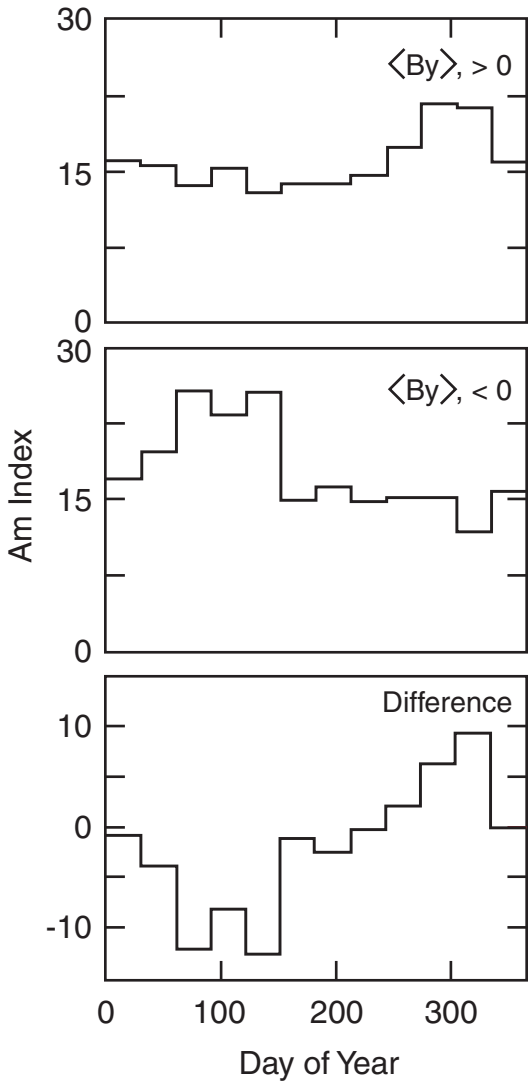
30
15
0
⟨By⟩, > 0
30
15
0
⟨By⟩, < 0
Am Index
10
0
-10
Difference
0
100
200
300
Day of Year

Figure 26

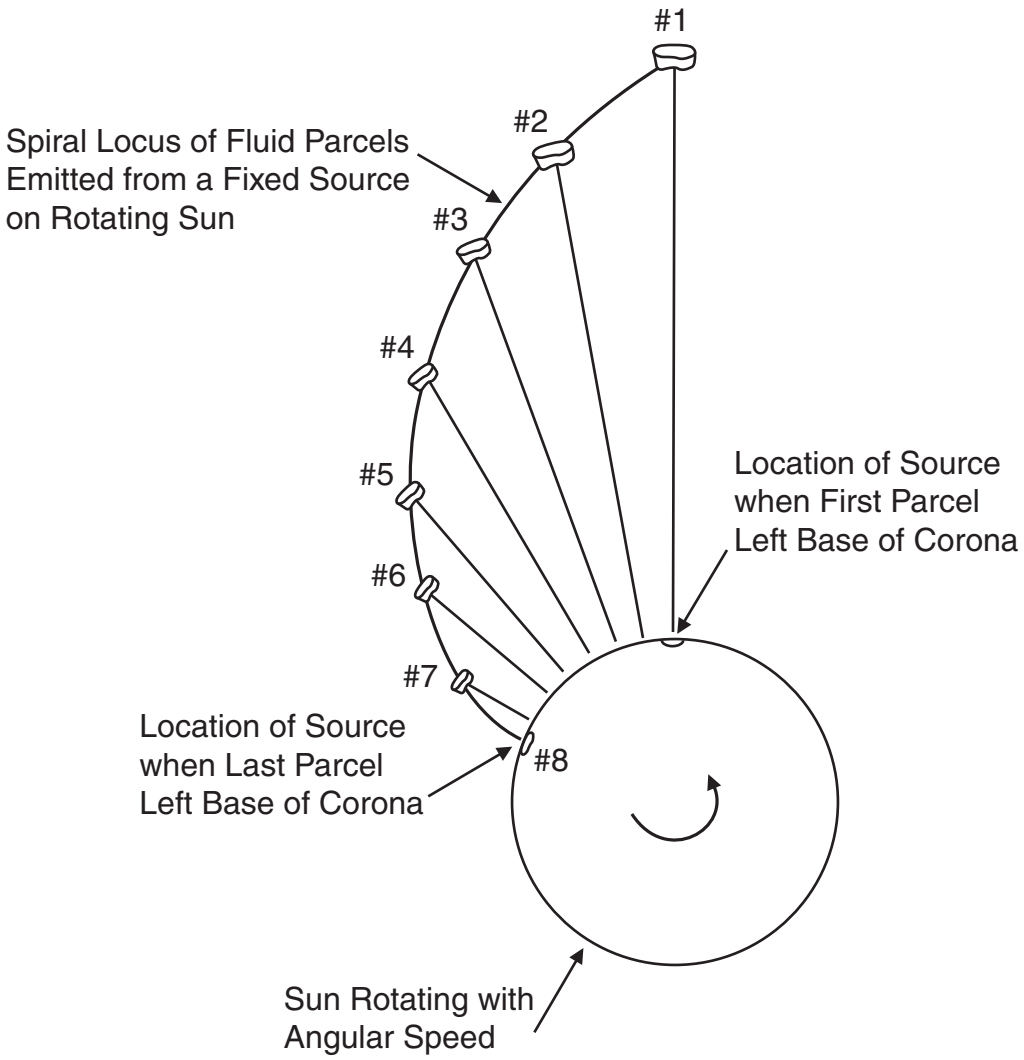
#1
#2
#3
#4
#5
#6
#7
#8
Spiral Locus of Fluid Parcels
Emitted from a Fixed Source
on Rotating Sun
Location of Source
when First Parcel
Left Base of Corona
Location of Source
when Last Parcel
Left Base of Corona
Sun Rotating with
Angular Speed

Figure 27

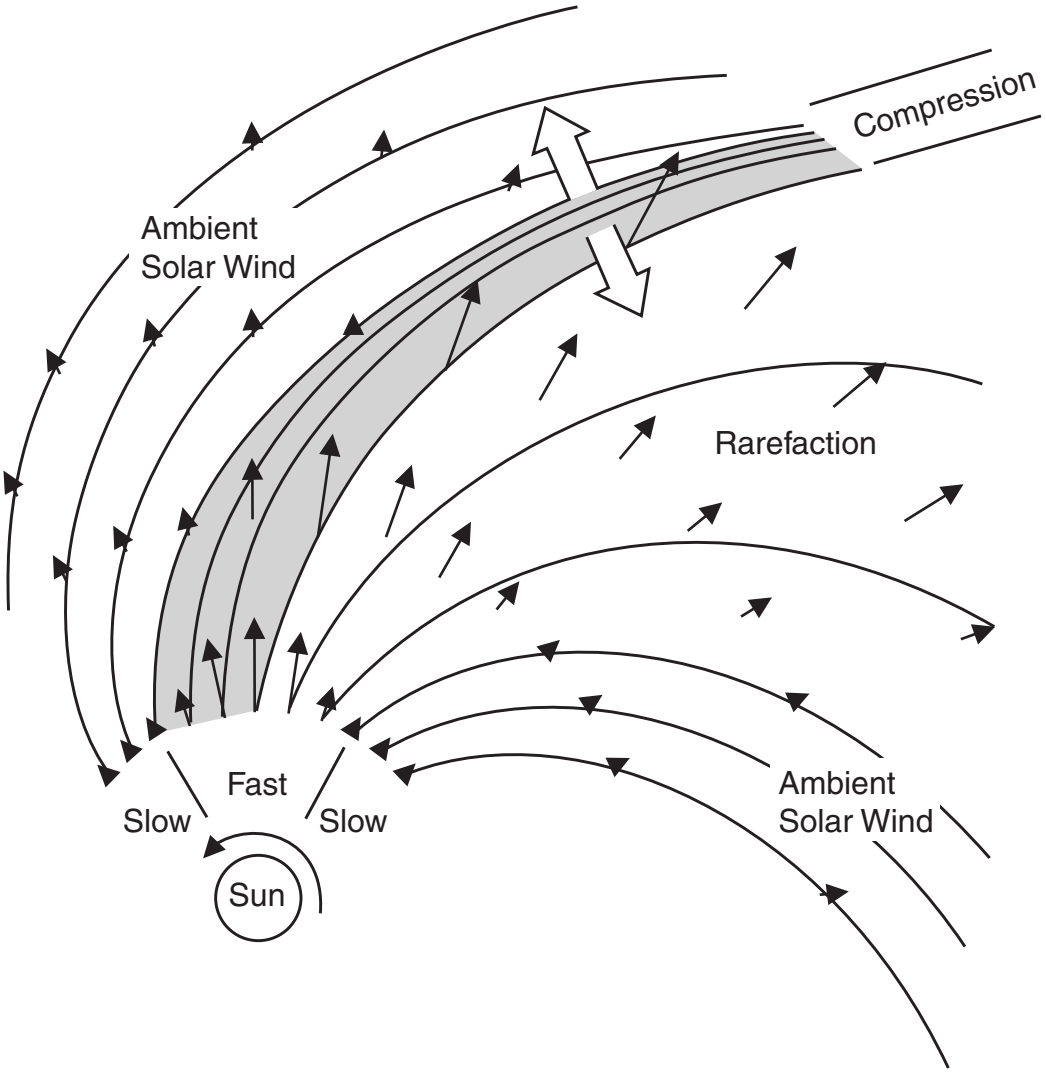
Compression
Ambient
Solar Wind
Rarefaction
Fast
Slow
Slow
Ambient
Solar Wind
Sun

Figure 28

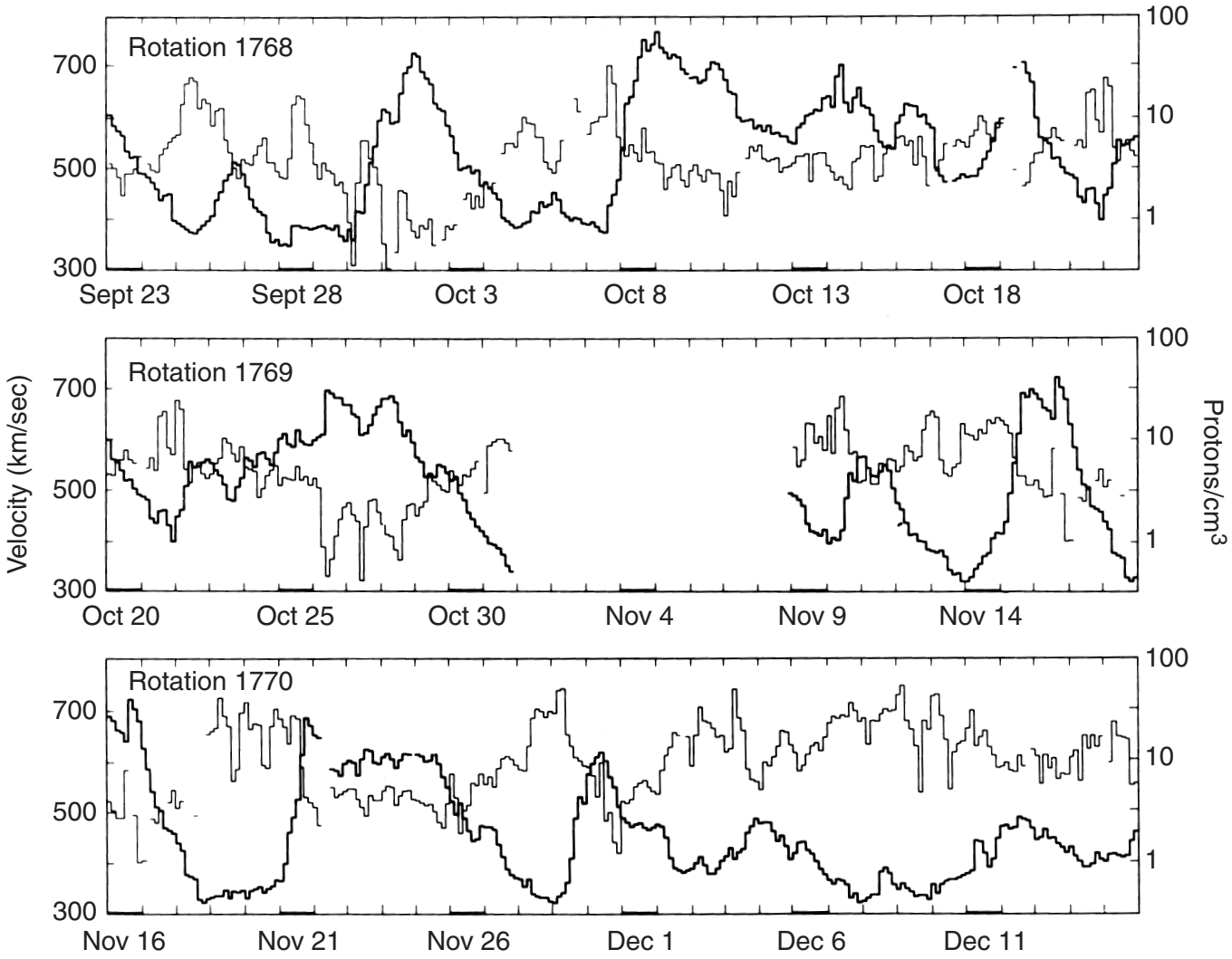
Rotation 1768
Rotation 1769
Rotation 1770
Velocity (km/sec)
Protons/cm3
700
500
300
100
10
1
Sept 23
Sept 28
Oct 3
Oct 8
Oct 13
Oct 18
Oct 20
Oct 25
Oct 30
Nov 4
Nov 9
Nov 14
Nov 16
Nov 21
Nov 26
Dec 1
Dec 6
Dec 11

Figure 29

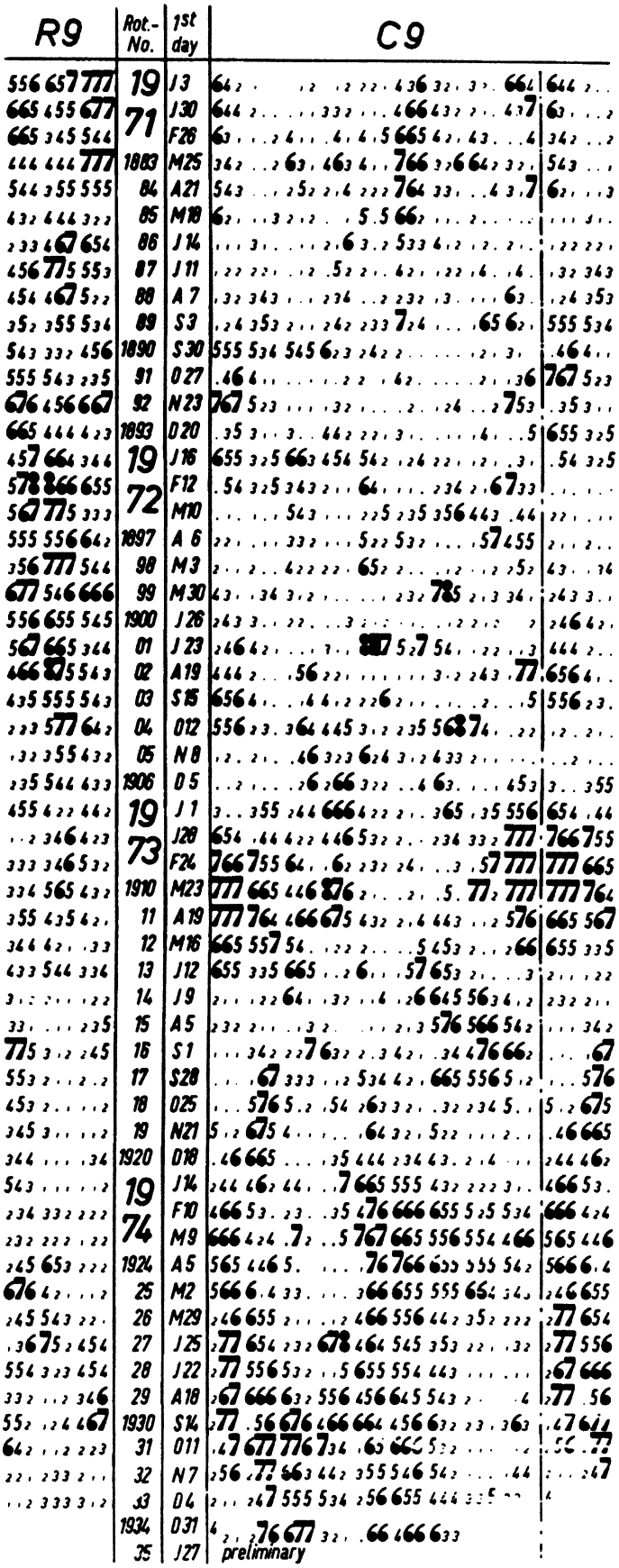

Symbol	.	,	2	3	4	5	6	7	8	∎
$\bar{R}$ =	0	1-15	16-30	31-45	46-60	61-80	81-100	101-130	131-170	171...
R9,C9 =	0	1	2	3	4	5	6	7	8	9
Cp =	0.0-0.1	0.2-0.3	0.4-0.5	0.6-0.7	0.8-0.9	1.0-1.1	1.2-1.4	1.5-1.8	1.9	2.0-2.5

Figure 30

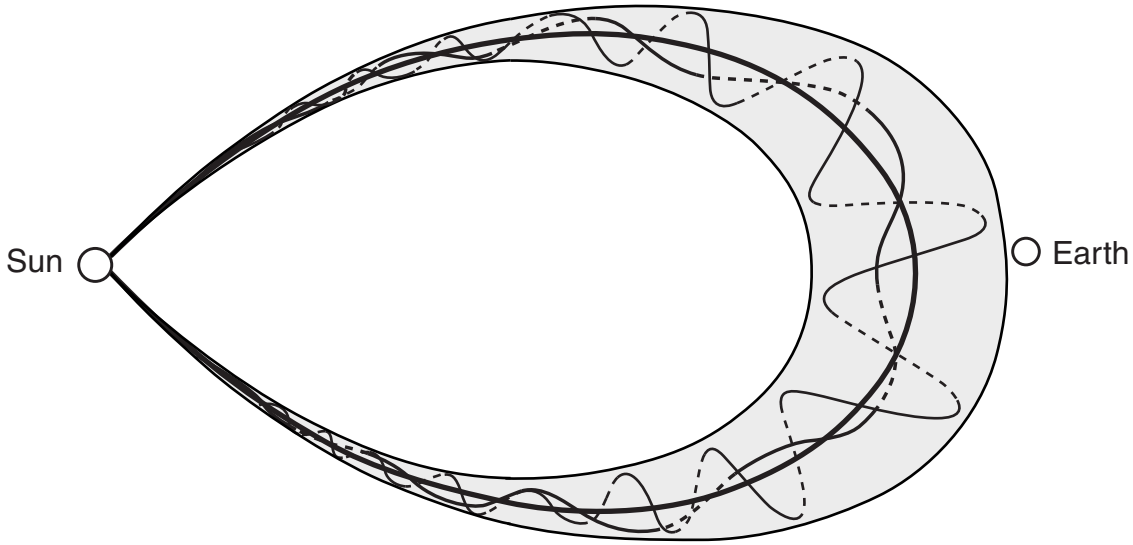

Figure 31

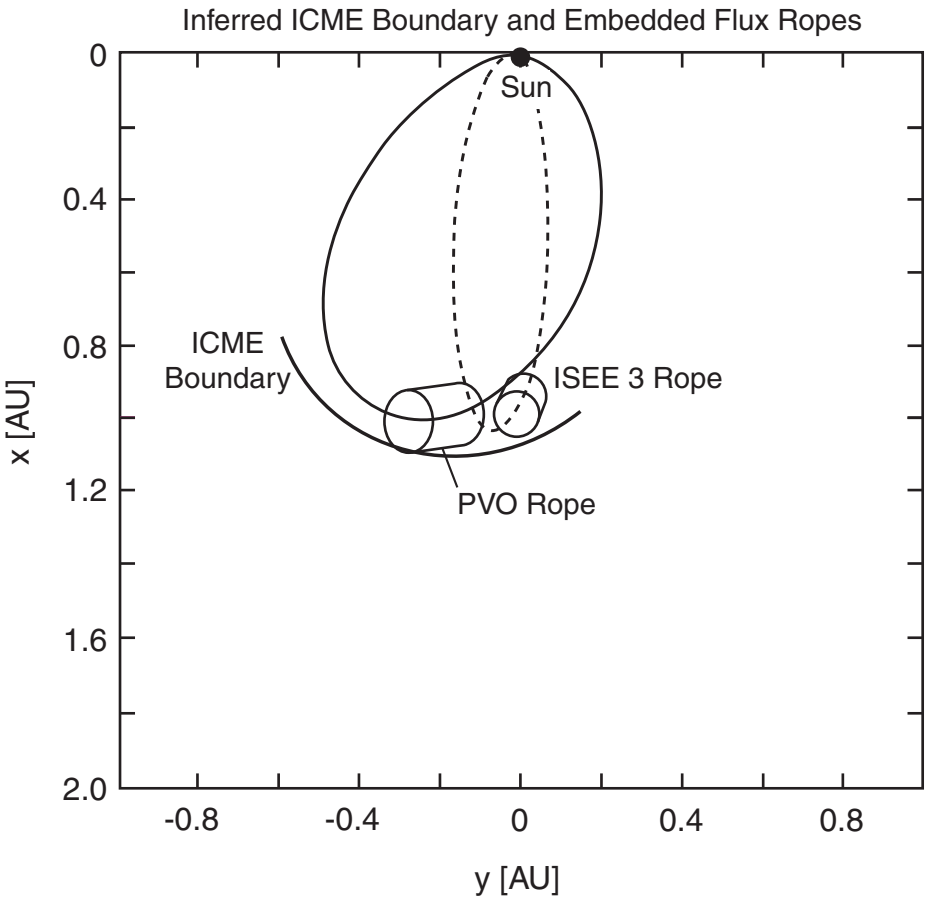
Inferred ICME Boundary and Embedded Flux Ropes
Sun
ICME
Boundary
ISEE 3 Rope
PVO Rope
x [AU]
y [AU]
0
0.4
0.8
1.2
1.6
2.0
-0.8
-0.4
0
0.4
0.8

Figure 32

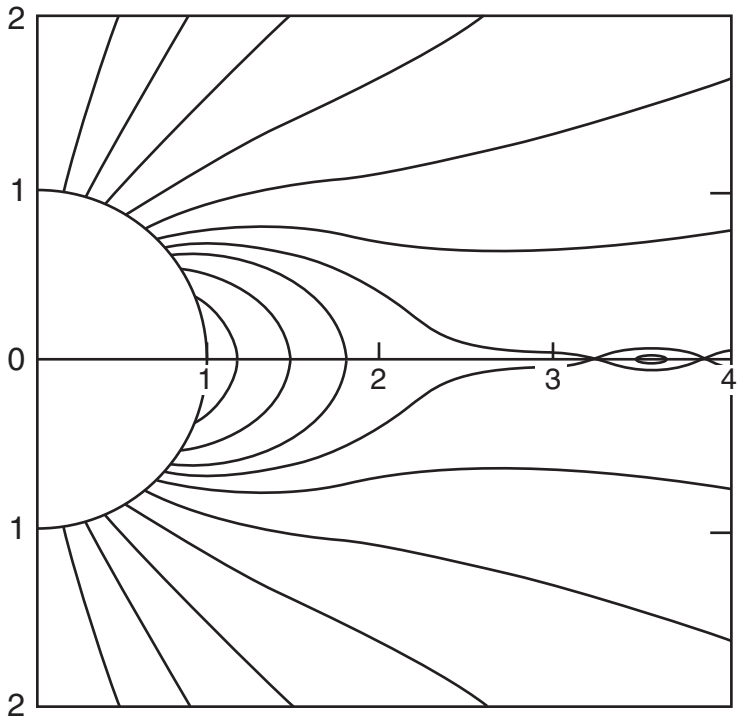

Figure 33

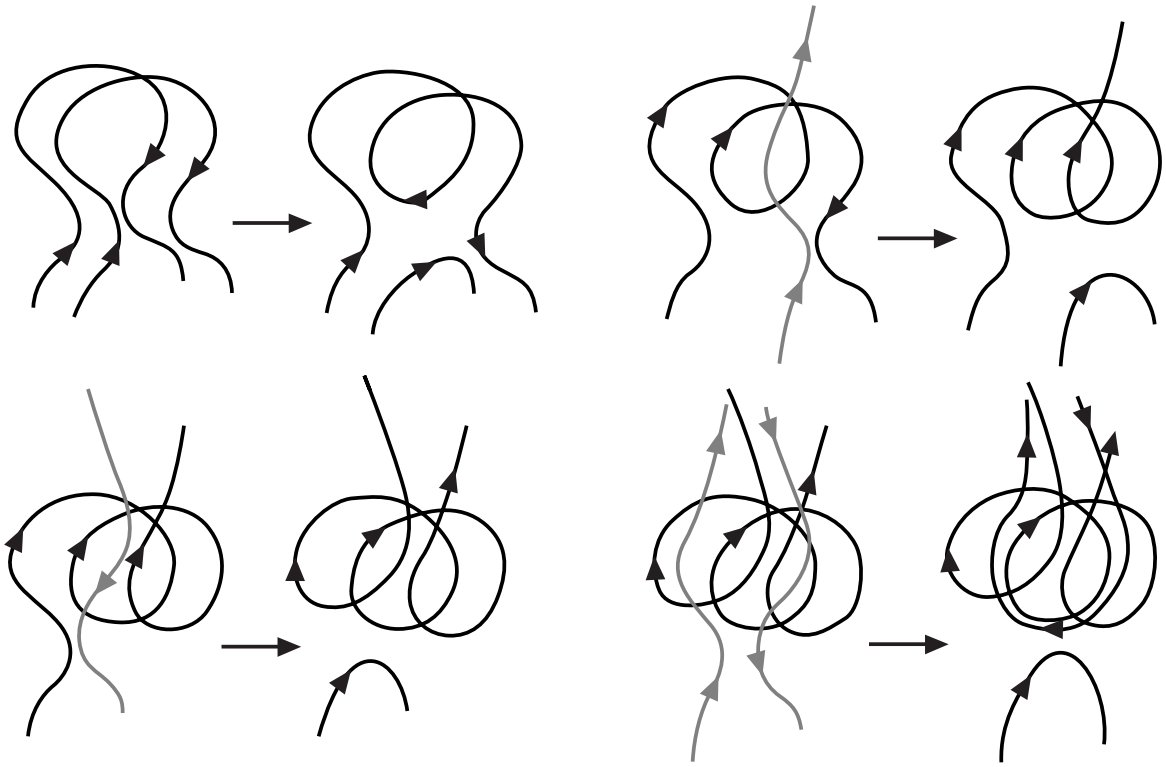

Figure 34

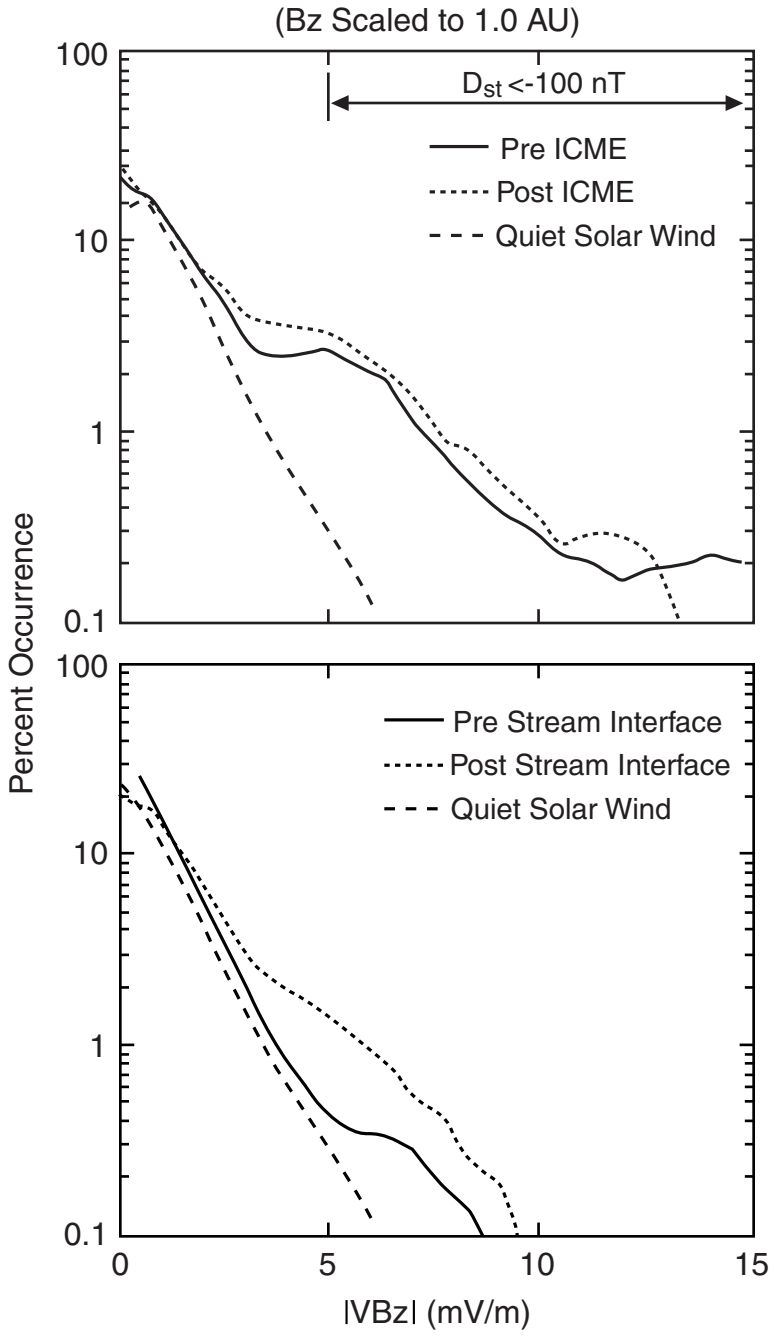
(Bz Scaled to 1.0 AU)
100
10
1
0.1
D_{st} <-100 nT
Pre ICME
Post ICME
Quiet Solar Wind
Percent Occurrence
100
10
1
0.1
Pre Stream Interface
Post Stream Interface
Quiet Solar Wind
0
5
10
15
|VBz| (mV/m)

Figure 35